

NASA Langley Research Center

Geostationary Tropospheric Pollution Satellite (Geo Tropsat)

Alan Little, Robert Estes, Doreen Neil, and David Rosenbaum
Langley Research Center, Hampton, Virginia
Nurul Abedin
Science Applications Int., Corp., Hampton, Virginia

System Study Report **Version 1.3**

December 16, 1998

Table of Contents

List of Tables	iv
List of Figures.....	v
Definitions / Acronyms	vi
1. Objectives and Methodology	1-1
2. Science	2-1
2.1 Benefits of Geostationary Atmospheric Chemistry Measurements.....	2-1
2.2 Current State of Practice	2-1
2.3 Measurement Objectives.....	2-2
3. Measurement Concept	3-1
3.1 Operational Concept	3-2
3.2 Mission Requirements.....	3-3
3.2.1 Signal-To-Noise Ratio.....	3-3
3.2.2 Orbital Requirements	3-6
3.2.3 Orbital Environment	3-6
3.2.4 Operational Life	3-7
3.2.5 Wavelength	3-7
3.2.6 Attitude Control.....	3-8
3.2.7 CO Sensor Pointing Requirements.....	3-8
3.2.8 Position Knowledge.....	3-9
3.2.9 Geolocation.....	3-9
3.2.10 Spatial Resolution	3-9
3.2.11 Temporal Resolution	3-10
3.2.12 Field of View	3-10
3.2.13 CO Sensor Dynamic Range.....	3-10
3.2.14 Filters	3-10
3.2.15 Autonomous Operation	3-11
3.2.16 Data Rate and Data Downlink.....	3-11
3.2.17 On-orbit Calibration	3-11
3.3 Programmatic Requirements.....	3-11
3.3.1 Payload Development Time	3-11
3.3.2 On-Orbit Operations.....	3-12
3.3.3 Ground Operations.....	3-12
3.3.4 Operational Lifespan.....	3-12
4. Mission Description	4-1
4.1 System Trade-offs.....	4-1
4.1.1 Dedicated Satellite Vs Piggyback.....	4-1
4.1.2 Orbital Position and Number of Satellites.....	4-2
4.1.3 Downlink.....	4-4
4.1.4 Command and Control	4-5
4.2 Instrument Trades	4-6
4.2.1 Backplane Architecture vs. Stand-Alone Single Board Computer.....	4-7
4.2.2 Mongoose V CPU vs. RAD6000 CPU.....	4-7

4.2.3	Power	4-8
4.2.4	IR FPA Selection.....	4-8
4.2.5	CO Sensor Wavelengths.....	4-11
4.2.6	Single Vs Dual Integration.....	4-12
4.2.7	Gas Cell Length.....	4-13
4.2.8	Ozone Sensor Wavelengths	4-14
4.2.9	UV CCD Selection.....	4-14
5.	Technology Assessment.....	5-1
5.1	IR FPA	5-1
5.2	UV-Visible CCD	5-2
5.3	Electronics	5-2
5.4	Thermal	5-3
5.5	Software.....	5-3
6.	Conclusions and Recommendations.....	6-1
7.	Appendix A -- Focal Plane Array (FPA) Technologies.....	7-1
7.1.1	Thermal Detectors.....	7-1
7.1.2	Quantum Detectors.....	7-2
7.2	Discussion and Summary	7-13
7.3	FPA References.....	7-13
8.	Appendix B: Charge Coupled Devices (CCDs) for the UV - Visible Spectrum.....	8-1

List of Tables

Table 2-1. Anticipated Spaceflight Instrument Measurement Accuracy Goals.....	2-2
Table 3-1. Channel properties to measure tropospheric trace gases from a geostationary space platform	3-1
Table 3-2. Calculated Measurement Atmospheric Path Length and Required Signal to Noise Ratio at Spacecraft Solar Noon along the Spacecraft Longitude.....	3-4
Table 3-3. Signal to Noise Ratio as a Function of Airmass.....	3-5
Table 3-4. Ozone Sensor Wavelengths.....	3-8
Table 3-5. EOS Data Processing Level Definitions.....	3-12
Table 4-1. System Trades.....	4-1
Table 4-2. Instrument Trades	4-7
Table 4-3. Parameters Used for Single Vs Dual Integration Comparison.....	4-12
Table 4-4. Summary of Single/Dual Integration Comparison Results	4-13
Table 4-5. CCD Parameters	4-15
Table 4-6. Dark Current as a Function of Temperature.....	4-15
Table 4-7. Fast Frame Transfer Time.....	4-22
Table 5-1. Technology Capability Matrix	5-1
Table 8-1. Thermal Detector Performance and Operation Parameters	7-2
Table 8-2. Comparison of HgCdTe FPAs and GaAs/AlGaAs QWIP Parameters [A-21]	7-4
Table 8-3. Performance and Operation Parameters of Some Intrinsic Quantum Detectors [A-1].....	7-7
Table 8-4. Performance and Operation Parameters of Some Extrinsic Quantum Detectors [A-1].....	7-7
Table 8-5. IRCCD Detectors for Mid- and Long-Wavelength IR [A-1].....	7-8
Table 8-6. Comparison of IR imagers cost	7-8
Table 8-7. Comparison of different IR FPAs imagers and their materials with specifications, costs, and their manufacturers.....	7-10
Table 9-1. Comparison of CCDs' Performance Parameters, Costs, Delivery Time, and Vendors	8-2

List of Figures

Figure 3-1. A day in the life of Geo Tropsat	3-2
Figure 3-2. CO Sensor 15 Minute Data Sequence.....	3-3
Figure 3-3. Airmass as a function of season and latitude.....	3-5
Figure 3-4. Geo Tropsat constellation. Global coverage is provided by instruments located at 110°W, 10°E, and 130°E.	3-6
Figure 3-5. Yaw Calculation Geometry.....	3-9
Figure 3-6. Graphical Illustration of the Geo Tropsat Field of View.....	3-10
Figure 4-1. View from 90°W.....	4-3
Figure 4-2. View from 70°W.....	4-3
Figure 4-3. Constellation of Three Satellites Located at 10°W, 130°W, and 250°W.....	4-4
Figure 4-4. Constellation of Four Satellites Located at 10°W, 100°W, 190°W, and 280°W.	4-4
Figure 4-5. TDRS Command and Control Option	4-6
Figure 4-6. CO Sensor Observation Parameters as a Function of Dark Current.....	4-10
Figure 4-7. CO Sensor Observation Parameters as a Function of Well Depth	4-11
Figure 4-8. Required Signal to Noise Ratio as a Function of Cell Length.....	4-14
Figure 4-9. Ozone Sensor Observation Parameters as a Function of Dark Current....	4-18
Figure 4-10. Comparison of Ozone Sensor Observation Parameters as a Function of Temperature.	4-19
Figure 4-11. Comparison of Ozone Sensor Observation Time as a Function of Temperature (log scale)	4-20
Figure 4-12. Comparison of Ozone Sensor Observation Time as a Function of Temperature	4-21

Definitions / Acronyms

Acronym	Definition
ABLE-2A	Amazon Boundary Layer Experiment 2A
ACE	Aerosol Characterization Experiment
ACS	Advanced Camera System
AGS	Advanced Geosynchronous Office
APD	Avalanche PhotoDiode
ASIC	Application Specific Integrated Circuit
AVHRR	Advanced Very High Resolution Radiometer
BSD	Board on Sustainable Development
C-C	Carbon-Carbon
CCD	Charge Coupled Device
CMAQ	Community Multi-scale Air Quality
CPCI	Compact PCI
COTS	Commercial Off The Shelf
CPU	Central Processing Unit
CTE	Charge Transfer Efficiency
DOE	Department of Energy
EMI	Electro-Magnetic Interference
EOS	Earth Observing System
EPA	Environmental Protection Agency
ESE	Earth Science Enterprise
FPA	Focal Plane Array
GEO	Geostationary Earth Orbit
Geo TropSat	Geostationary Tropospheric Pollution Satellite
GFCR	Gas Filter Correlation Radiometer
GLOBE	Global Learning and Observations to Benefit the Environment
GOES	Geostationary Operational Environmental Satellite
GSFC	Goddard Space Flight Center
GTE	Global Tropospheric Experiment
IBC	Impurity Band Conduction
IC	Instrument Controller
IGAC	International Global Atmospheric Chemistry Experiment
IGAP	International Global Aerosol Program
IR	Infrared
JPL	Jet Propulsion Laboratory
LaRC	Langley Research Center
LEO	Low Earth Orbit
LHB	Langley Handbook
LITE	Lidar In-space Technology Experiment
LWIR	Long Wave InfraRed
M5	Mongoose V
MAPS	Measurement of Pollution from Satellites
MCM	Multichip Module

Acronym	Definition
MIPS	Multiband Imaging Photometer
MOPITT	Measurements of Pollution in the Troposphere
MPP	Multi-Pinned Phase
MR Δ T	Minimum Resolvable Temperature Difference
NARSTO	North American Research Strategy for Tropospheric Ozone
NAS	National Academy of Sciences
NASA	National Aeronautics and Space Administration
NIR	Near InfraRed
NEP	Noise Equivalent Power
NE Δ T	Noise Equivalent Temperature Difference
NOAA	National Oceanic and Atmospheric Administration
NMP	New Millennium Program
PCB	Printed Circuit Board
PEM	Pacific Exploratory Mission
QWIP	Quantum Well Infrared Photodetector
RF	Radio Frequency
RMA	Rate Monotonic Analysis
RSDO	Rapid Spacecraft Development Office
RTOS	Real-Time Operating System
TDRS	Tracking and Data Relay Satellite
TOMS	Total Ozone Mapping Spectrometer
SAGE	Stratospheric Aerosol and Gas Experiment
SBC	Single Board Computer
SBRC	Santa Barbara Research Center
SBUV	Solar Backscatter UltraViolet
SCAR	Smoke, Clouds, and Radiation experiment
SIRTF	Space Infrared Telescope Facility
SNR	Signal to Noise Ratio
STIS	Space Telescope Imaging Spectrometer
SWIR	Short Wave InfraRed
UML	Unified Modeling Language
US	United States
UV	Ultraviolet

1. Objectives and Methodology

Geostationary imaging of trace constituents in the atmosphere represents a new capability for Earth sciences. This concept study was directed towards measurements of tropospheric carbon monoxide, nitrogen dioxide, and ozone with high temporal and spatial resolution to address NASA's Earth Science chemistry theme.

The objectives of this system study are to define a staring (i.e. non-scanning), ultraviolet-visible and near infrared, geostationary imaging radiometer for trace gas and aerosol measurement. Results of the study include the instrument parameters such as the required focal plane array sensitivity, integration times, channel parameters, and the technology required to build the instrument. The objective is to develop high sensitivity instrument capability requiring minimal cooling and with long life, low cost, and compact configuration. The availability of this sensor capability will eliminate the need for instrument active cooling, mechanical scanning, and will provide high resolution contiguous measurements over the regions of interest that will enable a new measurement capability of tropospheric trace gases.

A systems engineering process, in accordance with LHB 7122.1, was utilized to perform the system study. The systems engineering approach includes the identification of scientific and technical goals; the definition of system constraints and performance measures; and the analysis and development of system concepts. Instrument models were developed for each of the sensors and these models were utilized to perform trade studies to develop the system concept.

2. Science

2.1 *Benefits of Geostationary Atmospheric Chemistry Measurements*

The troposphere is a complex system. It comprises "point" and distributed sources of natural and anthropogenic origin; complicated transport processes, both lateral and vertical; and photochemistry driven by UV flux, temperature, atmospheric composition, and other variables. These sources, transport, and photochemical processes vary significantly in space and time. The best understanding of these processes requires observations that simultaneously possess high spatial and temporal resolution, which are uniquely available from geostationary orbit. Efforts have been made to provide high spatial resolution (10 x 10 km) from low Earth orbit (LEO), but the available temporal resolution from LEO (1 day or more) is inadequate to understand crucial processes which have time scales of minutes or hours. In addition, the "global" picture obtained from LEO (even for instruments that revisit the same spot on Earth every 24 hours) is a convolution of the true, but rapidly changing, tropospheric state. The LEO perspective complicates the interpretation of the already complex troposphere.

GEO provides the ability to "stare" at a portion of Earth continuously. At GEO, the combination of continuous temporal access and recent advances in large 2-D imaging arrays provides high temporal and high spatial resolution required to advance tropospheric studies with accurate visualizations of source and transport processes. Geostationary measurements of trace gases provide an integrated observational strategy linking EOS low Earth orbit measurements of tropospheric chemistry, GOES operational measurements, and ground and aircraft regional surveys.

2.2 *Current State of Practice*

The Measurement of Air Pollution from Satellites (MAPS) experiment provided the first measurements of the global CO distribution from space. MAPS, a gas filter correlation radiometer, used separate single element detectors for each of three data channels. During its four missions on the Space Shuttle, MAPS made column-integrated measurements of CO in the 4.7 μm spectral region. The Geo TropSat system extends this technique significantly by developing an imaging system that uses multi-element detectors for all data channels.

The MOPITT instrument on EOS AM-1 extends the MAPS measurement technique by making measurements in three layers with a pressure modulated technique and uses the 2.3 and 4.7 μm spectral channels. MOPITT will revisit the same surface area every 14.5 days; in orbit the CO sensor would provide new data every 15 minutes over the observed area. MOPITT plans for a 22 km spatial footprint at nadir; the CO sensor would provide a 5.5 km footprint at nadir with the same 10 ppbv CO accuracy as MOPITT. If selected for a future science mission, the CO sensor would bring highly improved temporal resolution for trace gas measurements while maintaining the spatial resolution and accuracy of EOS.

Tropospheric ozone estimates have been obtained using the residuals technique of Fishman et al. Based on existing TOMS and SBUV satellite data. However, the TOMS and SBUV data must be gathered from separate satellites and spectral channels for these sensors are not optimized for retrieval of tropospheric ozone. This study addresses both the combination of TOMS and SBUV capability into one sensor, as well as the selection of spectral channels.

2.3 Measurement Objectives

The science spaceflight instrument measurement accuracies (goals) are shown in Table 2-1. An accurate instrument model, using measured system characteristics, rather than estimated parameters would enable highly credible sensitivity analyses for future science measurements. In addition, system performance data enhances efficient algorithm development.

Table 2-1. Anticipated Spaceflight Instrument Measurement Accuracy Goals

Temporal Resolution	Spatial Resolution	Measurement Accuracy
<ul style="list-style-type: none"> • 15 minute refresh of the entire viewed Earth disk provides identification of sub-hourly time scale processes. • Diurnal variations. • Seasonal trends. • Interannual variation. 	<ul style="list-style-type: none"> • 6 x 6 km nadir footprint identifies sources, sinks at local scale. • Combine pixels for regional scale processes. • Contiguous view of continents and oceans 	<ul style="list-style-type: none"> • CO accuracy same as EOS (10 ppbv CO). • CH₄ reference gas measurement • N₂O reference gas measurement • NO₂ accuracy 10% • Total column O₃ 5% • Enhanced boundary layer O₃ 20% • Cloud top height • Aerosol index
<ul style="list-style-type: none"> • Temporal sampling at least 96 times as frequently as EOS 	<ul style="list-style-type: none"> • 16x area resolution of EOS 	<ul style="list-style-type: none"> • Accuracy comparable to EOS

3. Measurement Concept

The CO sensor uses gas filter correlation radiometry (GFCR) to measure CO, as well as a reference gases, CH₄ and N₂O, in the infrared portion of the spectrum. MOPITT and MAPS use the GFCR technique for CO and CH₄ measurements. The CO Sensor is a filter wheel camera that uses an infrared FPA and gas cell filters on a constantly rotating filter wheel. The HgCdTe focal plane array identified in the system study provides 2,048 x 2,048 elements (4,194,304 simultaneous “sensors” targeted at Earth view). The measurement is made in two spectral bands located at 2.35 and 4.67 μm. The reference gases CH₄ and N₂O provide on-orbit cloud discrimination and increase the accuracy of the data retrievals for CO each each wavelength.

The ozone sensor measures solar backscatter in the near UV to visible spectral regions, to derive total ozone, stratospheric ozone, and aerosol density. The ozone sensor uses a 2,048 x 2,048 UV enhanced, thermoelectrically cooled, silicon CCD for 12 spectral channels. Wavelengths between 300 and 600 nm are determined by narrow interference filters positioned on a filter wheel in front of the CCD.

Analyses of performance of existing TOMS ozone and aerosol channels, SBUV, MAPS, and MOPITT channels guided the channel selection, which are shown in Table 3-1.

Table 3-1. Channel properties to measure tropospheric trace gases from a geostationary space platform

Channel	Wavelength	Bandwidth	Measurement	Required SNR at Min Radiance	Modeled SNR ¹	
					At Min Radiance ²	At Max Radiance
1	317.0 nm	1-2 nm	SO ₂ discrimination for column ozone retrieval	70	100.7	1,375.4
2	322.3 nm	1-2 nm	Column ozone	70	101.3	968.5
3	329 nm	1-2 nm	Column ozone	70	125.2	684.1
4	340 nm	1-2 nm	Aerosols/column ozone	70	131.3	696.6
5	390 nm	1-2 nm	Aerosols/ring effect (cloud height)	70	120.7	689.9
6	393.5 nm	1-2 nm	Aerosols/ring effect (cloud height)	70	116.6	698.9
7	435 nm	1-2 nm	NO ₂	70	105.4	852.1
8	438 nm	1-2 nm	NO ₂	70	109.5	696.3
9	441 nm	1-2 nm	NO ₂	70	107.8	696.0
10	511 nm	2-5 nm	Chappuis ozone	70	111.5	855.2
11	574 nm	2-5 nm	Chappuis ozone	70	109.9	1,090.8
12	600 nm	2-5 nm	Chappuis ozone	70	101.5	1,093.7
13	2350 nm	65 nm	CO, reference gas CH ₄	5,000	5,595	24,822
14	4670 nm	177 nm	CO, reference gas N ₂ O	2,000	2,056	22,923

- 1) Model used 2nm bandwidth for all channels except 393.5 nm, which was modeled at 1 nm bandwidth. Instrument aperture was 20 mm.
- 2) Minimum radiance is for 85 degree solar zenith angle with clear atmosphere and oceanic background. Maximum is 0 degree, cloud. SNR values result from frame summation.

Once the proposed measurement concepts are validated, the data can be used in conjunction with other tropospheric trace gas observations to lead to an understanding of both chemical and transport processes in the lower atmosphere. LEO observations that provide some vertical resolution in the troposphere will become more meaningful since they can then be interpreted in the context of the synoptic trace gas environment in which they were made.

3.1 Operational Concept

The instrument utilizes reflected sunlight to make the total column ozone, NO_x, and the lower tropospheric CO measurement. Thus the instrument acquires science data during the portions of the day where a section of the viewed area is illuminated by the sun. The nominal operational times are from 6:00 AM to 6:00 PM. During the remainder of the day, the instrument is in a standby by mode and performs the calibration sequences, dark current measurement, and I₀ measurement. A nominal 24-hour operational scenario is shown in Figure 3-1.

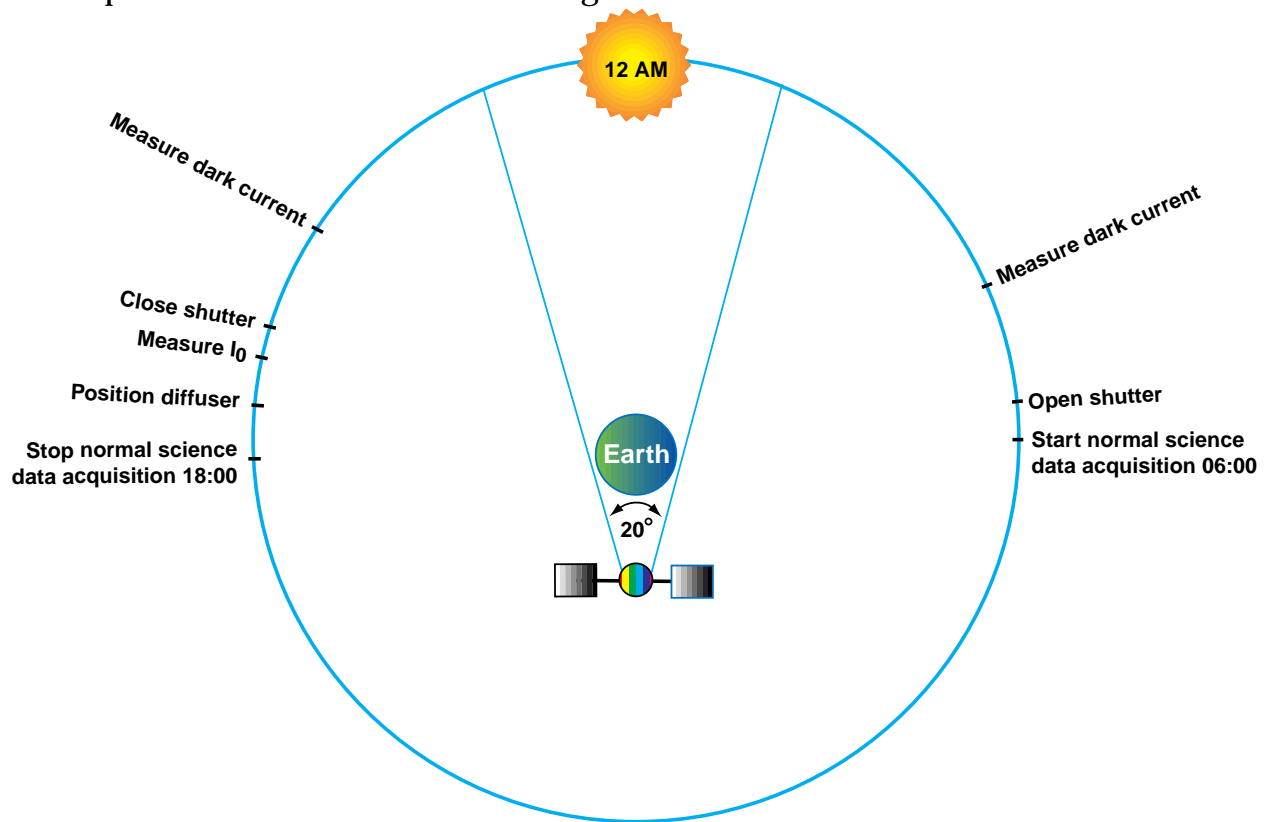
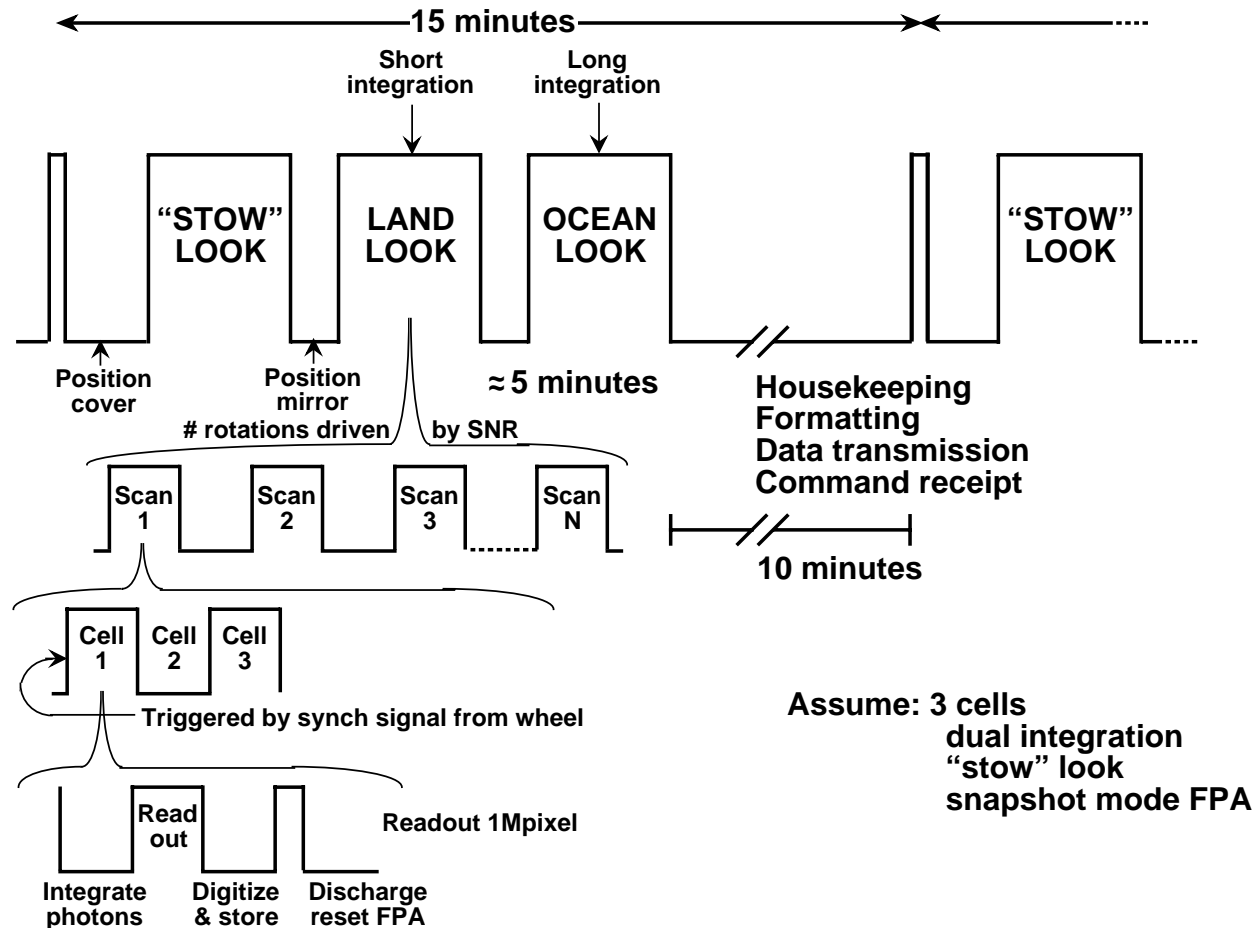


Figure 3-1. A day in the life of Geo Tropsat

The primary operating mode consists of a background level check (stow look), and two scene image sequences. The total image is divided in two (land and ocean) using the dual integration approach described in section 4.2.6. The image sequences consist of a series of snapshots through each of the six gas cells, which are summed on board, prior to being transmitted to the ground station. Enough images are summed to meet the required signal to noise requirements. A diagram of the 15 minute operating

scenario is shown in Figure 3-2. This sequence defines the operating mode and is repeated every 15 minutes during data taking operations.



al 12

Figure 3-2. CO Sensor 15 Minute Data Sequence

3.2 Mission Requirements

3.2.1 Signal-To-Noise Ratio

The single pixel signal to noise ratio (SNR) that is required to achieve a total column CO sensitivity of 10 ppbv is inversely related to the total atmospheric path length. The total atmospheric path length, A (in units of airmass), is that encountered by the incident and reflected solar radiation. The measurement airmass varies with the geographical location being imaged by any given pixel, the time of day, and the day of the year. Consequently the required SNR, (SNR_{req}), is pixel and time dependent. The SNR_{req} is expressed by the following equation:

$$SNR_{req} = \frac{12,130}{A} + 513.8$$

where,

A = airmass.

The measurement airmass is always greater than or equal to 2 and equals 2 for only one pixel (at the nadir point) at only two moments every year (spacecraft solar noon during the two equinoxes). Thus SNR_{req} is less than or equal to 6,579:1.

Table 3-2 contains airmass values, (A), and the required signal to noise ratio as a function of latitude along the spacecraft longitude for three times of the year (winter and summer solstice and the equinoxes) at spacecraft solar noon. These values represent the daily minimum measurement airmass and the corresponding daily maximum SNR_{req} along this longitude on these days of the year. For other longitudes the daily minimum airmass is greater and thus the SNR_{req} is less than the values presented in this table.

The SNR_{req} values in were calculated assuming the following CO correlation cell parameters: cell path length equal to 80 mm, cell temperature equal to 263K, and cell pressure equal to 1,000 mb. A significant (~30%) reduction in the SNR_{req} may be achieved in future CO imager designs by using a longer correlation cell path length. Table 3-3 shows the signal to noise ratio as a function of airmass. Figure 3-3 shows airmass as a function of latitude and season.

Table 3-2. Calculated Measurement Atmospheric Path Length and Required Signal to Noise Ratio at Spacecraft Solar Noon along the Spacecraft Longitude.

Calculated Atmospheric Path Length and Required Signal to Noise Ratio at Spacecraft Solar Noon Along the Spacecraft Longitude.						
Latitude (deg)	Winter Solstice Atmospheric Path Length		Equinox Atmospheric Path Length		Summer Solstice Atmospheric Path Length	
	Airmass	SNR_{req}	Airmass	SNR_{req}	Airmass	SNR_{req}
-80	4.135	3,447	27.682	952	NA	NA
-70	3.196	4,310	7.809	2,067	NA	NA
-60	2.663	5,068	4.654	3,120	34.035	870
-50	2.340	5,697	3.401	4,081	8.142	2,004
-40	2.145	6,170	2.750	4,925	4.705	3,092
-30	2.038	6,466	2.374	5,623	3.399	4,083
-20	2.003	6,569	2.154	6,146	2.738	4,944
-10	2.038	6,466	2.037	6,469	2.365	5,643
0	2.150	6,155	2.000	6,579	2.150	6,155
10	2.365	5,643	2.037	6,469	2.038	6,466
20	2.738	4,944	2.154	6,146	2.003	6,569
30	3.399	4,083	2.374	5,623	2.038	6,466
40	4.705	3,092	2.750	4,925	2.145	6,170
50	8.142	2,004	3.401	4,081	2.340	5,697
60	34.035	870	4.654	3,120	2.663	5,068
70	NA	NA	7.809	2,067	3.196	4,310
80	NA	NA	27.682	952	4.135	3,447

Table 3-3. Signal to Noise Ratio as a Function of Airmass

SNR as a Function of Airmass	
Airmass	Required Signal to Noise Ratio
2.1	6,290
2.5	5,366
3.0	4,557
4.0	3,546
5.0	2,940
6.0	2,535
10.0	1,727

**Minimum Airmass
as a Function of Latitude and Time of Year**

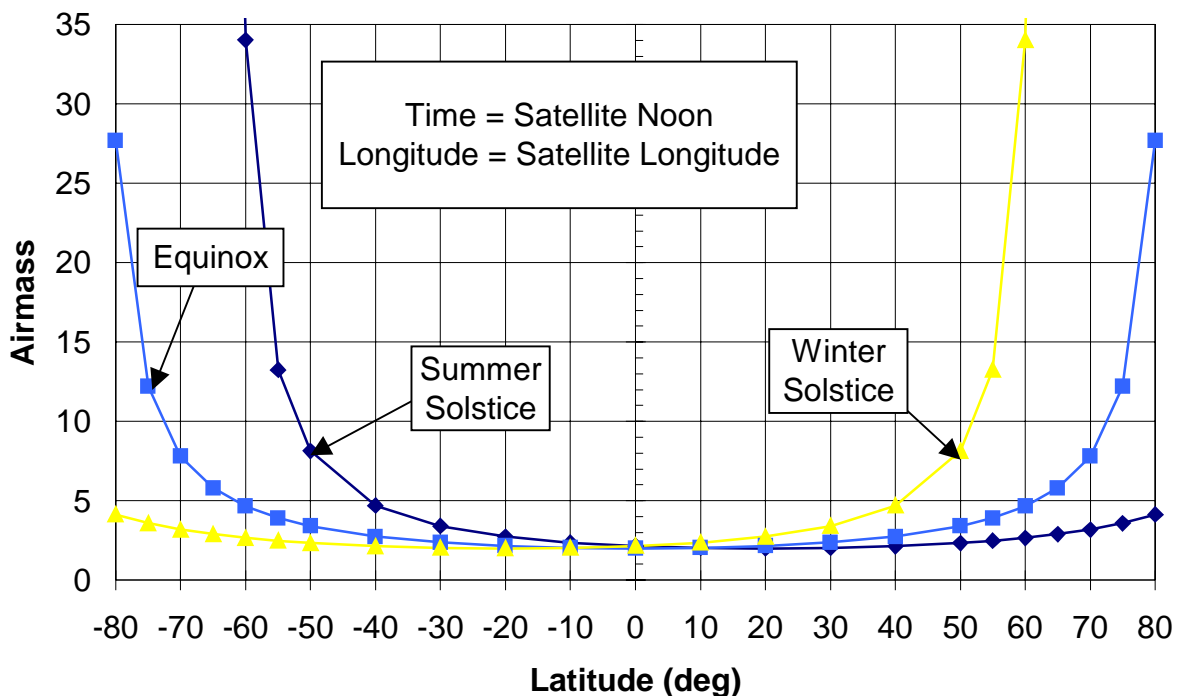


Figure 3-3. Airmass as a function of season and latitude.

The ozone sensor functional requirements specify a total column O_3 measurement with 1% accuracy, a stratospheric O_3 measurement with 1% accuracy, and a derived tropospheric O_3 measurement with 10% accuracy. The total column O_3 accuracy is achieved in the Cluster 1 ozone bands (Table 3-4) with a mean signal to noise ratio of 1,000 at the mean radiance of $33 \text{ W/cm}^2\text{-sr}$ at 312 nm. The minimum scene radiance of $0.4 \text{ W/cm}^2\text{-sr}$ occurs at 308 nm near the band used for stratospheric

O₃ measurement. The corresponding signal to noise ratio is 60 and this will define the number of samples needed to achieve the desired 1% accuracy. The stratospheric ozone distribution is relatively uniform. The maximum scene radiance is estimated to be 308 W/cm⁻¹-sr defining the dynamic range of the instrument.

3.2.2 Orbital Requirements

The payload is designed to operate in geostationary orbit. The mission is designed around a constellation of 3 geostationary satellites nominally spaced 120° apart, which observes the entire globe as shown in Figure 3-4.

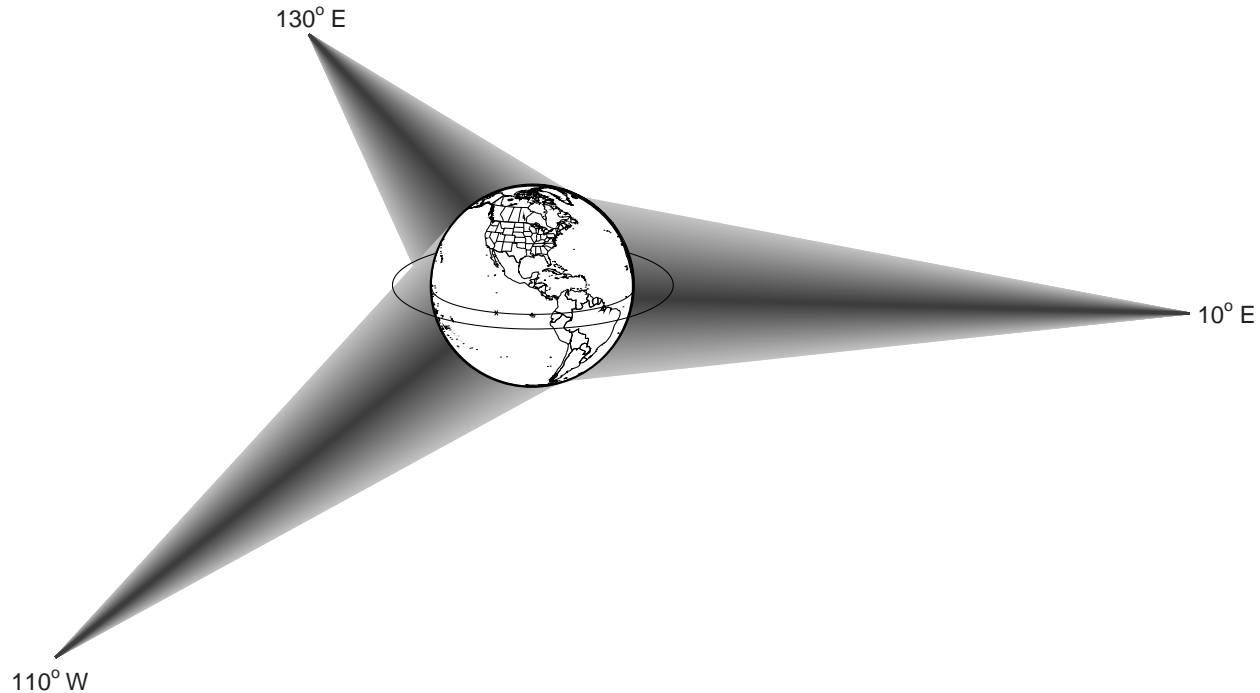


Figure 3-4. Geo Tropsat constellation. Global coverage is provided by instruments located at 110°W, 10°E, and 130°E.

3.2.3 Orbital Environment

The payload will be exposed to four distinct environments during its lifetime: Ground Environment, Launch Environment, Transfer Orbit Environment, and On-orbit Environment. The first three of these are either typical environments or transitional with the payload in a secure mode. The On-orbit Environment is the primary concern since the conditions in geostationary orbit are somewhat different from low Earth orbit. The principle environmental factors will be briefly discussed here with the planned rationale for Geo Tropsat. On-orbit mechanical environments are not expected to be severe. The spacecraft will experience continual pitch rotation to maintain its nadir orientation plus periodic jitter motion resulting from solar panel adjustments. Infrequent station-keeping maneuvers may also result in mechanical motions. The payload will be designed to accommodate these disturbances. The payload thermal environment will be severe due to continuously changing sun angle with respect to the

spacecraft. The payload design will accommodate the thermal extremes and will provide protection against direct solar exposure of the optical subsystem. On-orbit particulate exposure from high energy electrons and protons, cosmic particles, and low energy particles will result in a significant radiation exposure over the life of the payload. The Geo Tropsat design will utilize radiation resistant materials and components when possible and will employ localized radiation shielding to protect sensitive components such as the focal plane arrays. Contamination control will be an emphasis throughout the life cycle of the payload as well as on-orbit. The payload design will minimize the use of non-metallic materials that might generate volatile condensable materials and metallic materials that might become sources of particulate contamination. The spacecraft and launch vehicle shroud are controlled to a product cleanliness level of 550A per MIL-STD-1246C. The instrument internal cleanliness will be controlled to a level of 300A to maintain instrument performance over the spectral range of interest from the near ultraviolet to the mid infrared. This level will be maintained by closing the payload, and purging when possible, when installed on the spacecraft and by delaying the on-orbit operation until the spacecraft has been allowed to outgas. On-orbit contamination from the spacecraft ion propulsion attitude control system is expected to be negligible. Internal operational contamination from payload moving parts such as filter wheels, shutters, and positioning devices will be controlled by stringent cleanliness controls during assembly and by the use of sealed bearings and devices requiring the use of approved space lubricants.

3.2.4 Operational Life

The payload will be designed for two years of operations with options for up to three additional years in yearly increments. Two years of operations from geostationary orbit will enable the quantification of both seasonal and interannual variations. The payload will be turned off by the spacecraft owner/operator, once the spacecraft performance capabilities have degraded to the point where there is insufficient margin to run the Geo Tropsat payload without interfering with the satellite's primary communications functions.

3.2.5 Wavelength

3.2.5.1 CO Sensor Wavelengths

The CO sensor will have two channels, 2.35 μm , and 4.67 μm .

3.2.5.2 Ozone Sensor Wavelengths

The ozone sensor has 12 active channels as shown in Table 3-4. The channels are grouped in clusters and are enumerated in their relative measurement priority. Two additional "channels" are utilized for instrument in-flight verification; a blank opaque position for dark current measurements and array artificial illumination and a clear position for solar illumination from an external solar diffuser plate. These wavelengths are subject to further review.

Table 3-4. Ozone Sensor Wavelengths

Ozone Sensor Wavelengths			
Cluster Number	Spectral Range (nm)	Number of Channels	Function
1	300-360	5	Total ozone, SO ₂ , aerosols, reflectivity
2	295-305	1	Upper level ozone, volcanic cloud height
3	390-410	2	Cloud top height
4	500-600	3	Chappuis band total ozone
5	740-760	1	Sulfate aerosols

3.2.6 Attitude Control

No provision will be made to control the attitude of the spacecraft in order to control the pointing of either the carbon monoxide sensor or the ozone sensor. A separate control subsystem may be provided to control the pointing of the CO sensor, in addition to the spacecraft attitude control system. Commercial communications spacecraft attitude control systems maintain the spacecraft's attitude to within 0.1 degrees in the roll and pitch axes, and 0.25 degrees in the yaw axis.

3.2.7 CO Sensor Pointing Requirements

The CO measurements are made by differencing two large, similar numbers (CO - Vacuum and CH₄ - Vacuum) that are acquired sequentially and averaged until the desired signal to noise ratio has been achieved. The scene between image acquisitions can change by either motion of the spacecraft or movement of a scene feature (i.e., a cloud). In order to be certain that the observed scene for the two sequentially acquired images are the same, a gas cell pair pointing requirement is required. This cell to cell requirement has been set at 0.1 km based on calculations that show the image of a small scene feature change. Another requirement arises from the stated spatial resolution. The total pointing change that is acceptable to avoid degrading the spatial resolution has been set at 20% of the spatial resolution or 1 km.

3.2.7.1 CO Sensor Pitch and Roll Pointing Requirements

The pitch and roll pointing requirements are as follows:

- 0.1 km for 1 gas cell pair (approximately 0.02 seconds) $\Delta\theta \leq \frac{0.1 \text{ km}}{35,800 \text{ km}} = 2.79 \mu\text{radians}$
- 1 km for entire image (approximately 180 seconds) $\Delta\theta \leq \frac{1 \text{ km}}{35,800 \text{ km}} = 27 \mu\text{radians}$.

3.2.7.2 CO Sensor Yaw Pointing Requirements

The length of the arc between the nadir view point and a point on the rim of the Earth is given by the following equation with the geometry shown in Figure 3-5.

$$\text{arc} = R_e \cdot (\alpha_{\text{rim}} - \alpha_{\text{nadir}})$$

where,

R_e = Radius of the Earth = 6378 km

α_{rim} = Tangential viewing angle = 1.382 radians (79.2 degrees)

α_{nadir} = Nadir viewing angle = 0 radians (0 degrees)

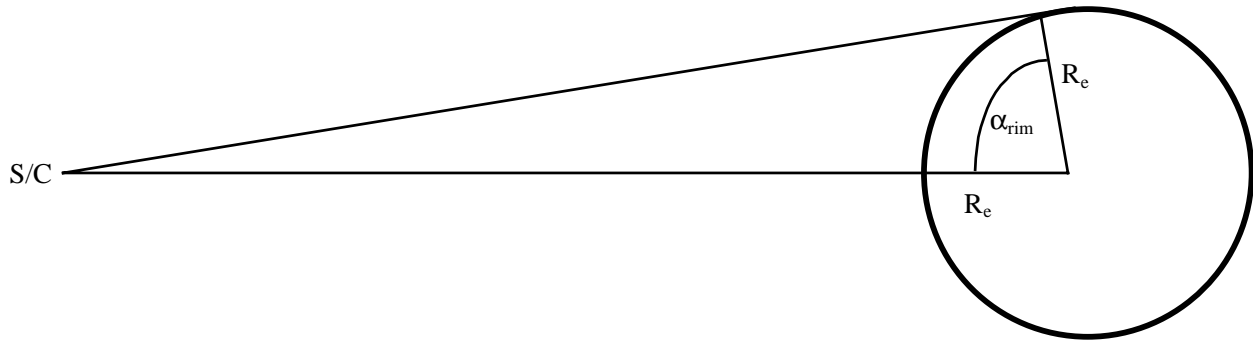


Figure 3-5. Yaw Calculation Geometry

- 0.1 km for 1 gas cell pair (approximately 0.02 seconds), $\Delta\theta \leq \frac{0.1}{R_e \cdot (\alpha_{rim} - \alpha_{nadir})} = 11.3$ μ radians.
- 1 km for entire image (approximately 180 seconds), $\Delta\theta \leq \frac{1}{R_e \cdot (\alpha_{rim} - \alpha_{nadir})} = 114$ μ radians.

3.2.8 Position Knowledge

The location of the spacecraft will be provided by the spacecraft operator to the payload ground operations team.

3.2.9 Geolocation

Additional pointing knowledge can be derived from the data stream is required to geolocate the two science data sets (CO, NO₂, and O₃) to 1km. Geolocation is required to accurately locate and identify CO, NO₂, and O₃ sources and sinks.

3.2.10 Spatial Resolution

The desired ground spot diameter is 6 km at nadir to accurately image plumes and determines the location of sources and sinks. This spatial resolution will allow for multiple pixels in large urban areas. Unlike LEO, the ground spot diameter increases as the distance from the nadir increases for all geostationary observations. A 6 x 6 km footprint identifies sources and sinks at local scale.

3.2.11 Temporal Resolution

The desired temporal resolution is 15 minutes. A 15 minute refresh rate provides identification of hourly time scale processes, diurnal variations, seasonal trends, and interannual variation.

3.2.12 Field of View

The two sensors should be coaligned and view the entire disk, shown in Figure 3-6, with sufficient margin to account for spacecraft motion. Thus the full angle field of view (FOV) is set at 0.314 radians (18.0°). The number of detector pixels sets the instantaneous field of view (IFOV) (2,048) and the FOV. Thus, the IFOV equals 154 μradians, which corresponds to a ground spot distance of 5.5 km at nadir. The field of view of the two sensors is identical.

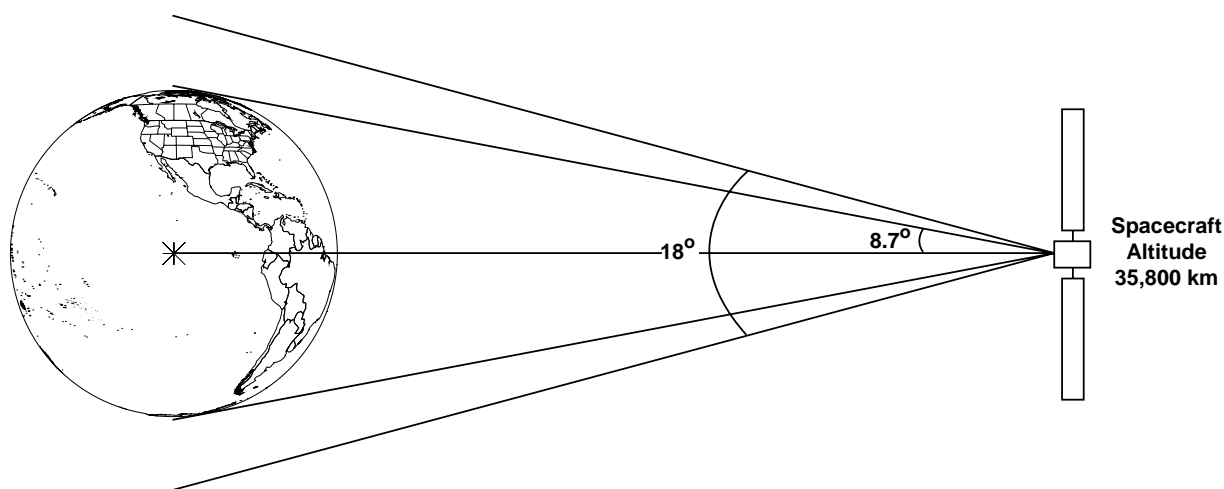


Figure 3-6. Graphical Illustration of the Geo Tropsat Field of View

3.2.13 CO Sensor Dynamic Range

The scene dynamic range is expected to be approximately 50. The albedo of the ocean is 0.02, and the albedo of clouds is approximately 0.2 to 0.6. The solar flux, reflected from the ocean is 1.87×10^{-13} watts/pixel when the solar zenith angle is 0° and is 2.03×10^{-14} watts/pixel when the solar zenith angle is 85° . The solar flux is a function of the solar zenith angle and varies by approximately a factor of 9 diurnally. The required electronics dynamic range is given by the equation below.

$$\text{dynamic range} = dr_{\text{flux}} \cdot dr_{\text{scene}} \cdot dr_{\text{ADC}} = 1.84 \times 10^6$$

where,

dr_{flux} = diurnal solar flux dynamic range = 9,

dr_{scene} = scene dynamic range = 50,

and dr_{ADC} = ADC dynamic range = 2^{12} .

3.2.14 Filters

A narrowband optical filter(s) should be provided to set the spectral bandpass of the sensors. Provisions should be made to maintain the filter at a constant, known

temperature, and as low as practicable temperature. The filters should provide out-of-band rejection of 10^8 .

3.2.15 Autonomous Operation

The payload will be designed to operate autonomously and provide both on-orbit flexibility and modifiability. The maximum payload command rate shall be one command block per week. The instrument shall be capable of executing a predetermined number of stored payload command profiles. In addition parameters necessary to perform payload operations shall be stored in tables. Both the payload command language routines and the payload operations parameter tables shall be modifiable in orbit.

3.2.16 Data Rate and Data Downlink

The downlink and ground station should have enough bandwidth to accommodate the volume of data from both sensors.

3.2.16.1 Data Formatting

Several formats are available for use and can simplify ground operations if significant software is available for reuse. Many NASA experiments in the EOS era are using the Consultative Committee on Space Data Systems (CCSDS) format. Geo TropSat will evaluate protocols and formats for data downlink.

3.2.17 On-orbit Calibration

3.2.17.1 CO Sensor Calibration System

The CO sensor will incorporate a two-point stable blackbody measurement.

3.2.17.2 Ozone Sensor Calibration System

In-flight relative calibration of the focal plane array will be provided by three independent methods. Solar illumination of the array will be possible using a full aperture solar diffuser on the inside of the aperture door. This option will be available only at low relative solar angles, as at "sunset". The internal filter wheel will include an opaque blank position to block all array illumination to determine detector offsets and dark current effects. In this position, it will also be possible to activate an on-board LED for general illumination of the array to identify gross response changes in individual pixels.

3.3 Programmatic Requirements

3.3.1 Payload Development Time

Current NASA missions generally require the payload to be launched within three years from project start.

3.3.2 On-Orbit Operations

There will be two years of operations with options for up to three additional years in yearly options if the spacecraft and instruments perform adequately.

3.3.3 Ground Operations

Ground operations will assess the payload health and status, process the telemetered data to level 2, archive the data, and generate payload commands. The EOS data processing level definitions are shown in Table 3-5.

Table 3-5. EOS Data Processing Level Definitions

EOS Data Processing Level Definitions	
Level 0	Level 0 data products are reconstructed, unprocessed instrument/payload data at full resolution; any and all communications artifacts, e.g. synchronization frames, communications headers, duplicate data removed.
Level 1A	Level 1A data products are reconstructed, unprocessed instrument data at full resolution, time-referenced, and annotated with ancillary information, including radiometric and geometric calibration coefficients and georeferencing parameters, e.g., platform ephemeris, computed and appended but not applied to the Level 0 data
Level 1B	Level 1A data that have been processed to sensor units (not all instruments will have a Level 1B equivalent).
Level 2	Level 2 data products are derived geophysical variables at the same resolution and location as the Level 1 source data.
Level 3	Level 3 data products are variables mapped on uniform space-time grid scales, usually with some completeness and consistency.
Level 4	Level 4 data products are model output or results from analyses of lower level data, e.g. variables derived from multiple measurements.

3.3.4 Operational Lifespan

The sensor payload is designed for two years of on orbit operations.

4. Mission Description

4.1 System Trade-offs

This section provides a description of the major trade studies performed to arrive at the baseline system. Table 4-1 summarizes the major system trades.

Table 4-1. System Trades

Segment or Subsystem	Trade
Space	Dedicated satellite or commercial piggyback
Mission/Science	Orbital position, number of satellites
Downlink	Dedicated downlink or share comsat's
Command and Control	Dedicated uplink or share comsat's

4.1.1 Dedicated Satellite Vs Piggyback

This trade study examined the relative merits of a dedicated small GEO satellite versus piggybacking on commercial or government geostationary satellites. The Advanced Geosynchronous Studies (AGS) office at GSFC has been evaluating the feasibility of small GEO satellites and currently has two concepts (El Torito and a NRL design). The commercial space industry has assembled effective infrastructure to support geostationary communications and television systems. The commercial satellite could provide nadir view, electrical power, thermal environment, attitude, command uplink, and data downlink as on-orbit services for the secondary payload. Leasing these on-orbit services appears to be financially attractive to both NASA and the commercial satellite owners. Typically there are more than 25 successful new satellites in GEO annually potentially providing frequent opportunities for access to GEO. Global coverage for small payloads (multiple instruments) becomes fiscally possible with secondary payloads, and the international market provides flight opportunities around the globe. The single largest advantage of a piggyback approach is the reduced cost. A dedicated remote sensing GEO satellite costs approximately \$60-90M (RSDO catalog) including launch vehicle while a piggyback satellite ride to GEO can be obtained for approximately \$7-15M including 2 years of operations, based on discussions between LaRC and vendors.

Secondary payload status also imposes significant constraints on the science instrument. Physical size, mass, and schedule are the gatekeepers to successful secondary payload opportunities. On time delivery of the secondary payload is mandatory, and the commercial satellite will launch without the secondary payload in order to maintain schedule. The typical cycle time for commercial satellites is 24 months or less. The science instrument must be able to meet this schedule. Secondary payload status also means that the orbital location of the satellite is determined by commercial markets and not by the science payload. Desirable orbital locations can be obtained by surveying the market, selecting desirable options, and negotiating with the specific satellite license holders. Interaction with the commercial satellite operator is required to command the secondary payload, driving the science payload to be highly

autonomous (see section 4.1.4). One other concern with the use of communications satellites for science missions is the satellite pointing accuracy and stability. The science payload must be able to accept the coarse pointing capabilities or provide means to stabilize the instrument line of sight, which adds complexity and cost to the instrument. Occasionally, the secondary payload may endure a loss of power because of operational needs of the commercial payload. These constraints may be more relaxed on the government satellites although the operational nature of GOES and TDRS may place some operational restrictions on the secondary payload. Even with these constraints, secondary payloads at GEO afford enhanced science capability.

Studies undertaken by the AGS office have shown that small dedicated GEO satellites are feasible. The use of dedicated science platforms alleviates the secondary payload constraints but introduces additional concerns. Small dedicated GEO satellites require the development of a new satellite and all of the risks associated with the development. The project will also be responsible for all of the aspects of the mission. The cost is also significantly higher.

In summary the use of piggyback payloads on commercial communications provides an opportunity for significant cost savings. A piggyback payload costs between 1/5 and 1/10 of the cost of a dedicated satellite launch and uses a proven repeatable technical approach. This cost savings produces a dramatically higher science return per dollar.

4.1.2 Orbital Position and Number of Satellites

The satellite owner determines the orbital position of secondary payloads. The chosen orbital position affects the science that is conducted. Figure 4-1 and Figure 4-2 show the geometric footprints for two different orbital positions 70 and 90°W and lists some of the benefits and disadvantages of these locations. The figures also illustrate how the footprint of the sensor varies with distance from the nadir point. Global coverage requires multiple satellites. A constellation of three equally spaced satellites, as shown in Figure 3-4, provides global coverage however the footprints at the overlap regions are quite large. The footprints at the overlap region are between 15 and 25 km as shown in Figure 4-3. Also, as a practical matter, achieving an equally spaced constellation is not likely as a secondary payload. A constellation of three unequally spaced satellites would leave a portion of the Earth unviewed. Adding a fourth satellite to the constellation would allow for smaller footprints at the overlap regions as well as avoid any gaps in coverage due to uneven satellite spacing as shown in Figure 4-4. The footprints at the overlap region is between 8 and 10 km as shown in Figure 4-4. The primary limitation to the four satellite approach is the additional cost, although copies of an instrument can be built and tested at a reduced cost per instrument.

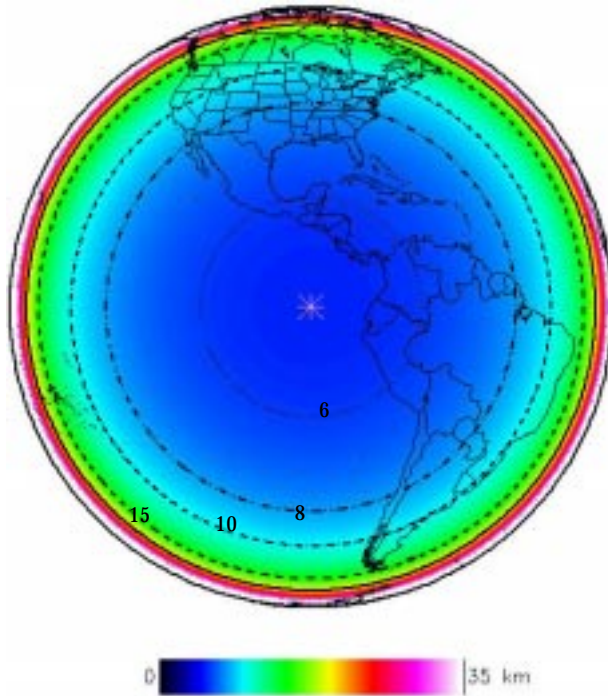


Figure 4-1. View from 90°W

- The nadir point (5.5 km) is located over the Galapagos Islands.
- All of the US (except the Pacific Northwest), and all Brazil are visible with footprints less than 10 km.
- Most of the US and Brazil are visible with footprints less than 15 km. 10-15 km footprints over the east coast, Los Angeles, and North American continental outflow.
- Footprint shape is nearly the same across the US.
- Less of the South Atlantic corridor is visible for observation of Africa - South America transport than for a sub-satellite position between 60-80 °W.
- Boreal emissions are available (15 km) up to Hudson Bay across North America.

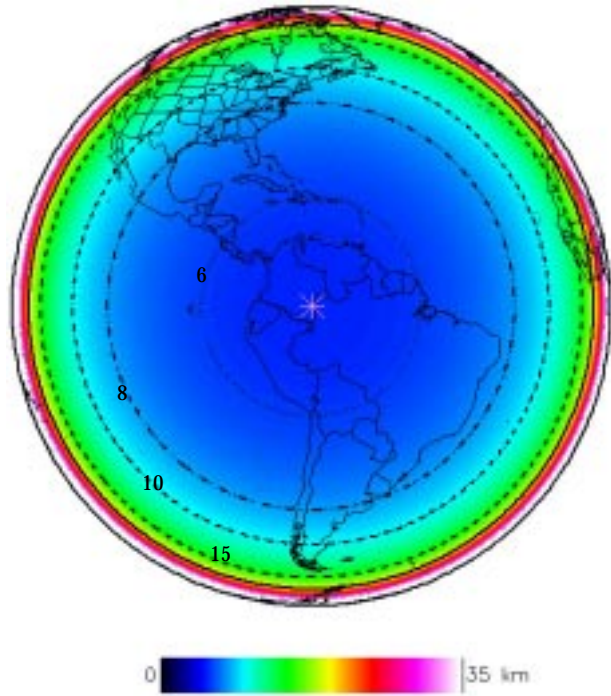


Figure 4-2. View from 70°W

- The nadir point (5.5 km) is located at the Columbia/Brazil border
- All of Brazil is visible with footprints less than 8 km. (Brazil is an important source of tropospheric pollutants, but has only sparse observation sites to measure these products.)
- Texas to New England can be observed with footprints less than 10 km. (Washington DC has a footprint less than 8 km.)
- Los Angeles and the Rocky Mountains have 15 km footprints. Consequently the size and shape of the pixels across the US varies by a factor of two.
- North American continental outflow and Africa - South America transport can be observed.

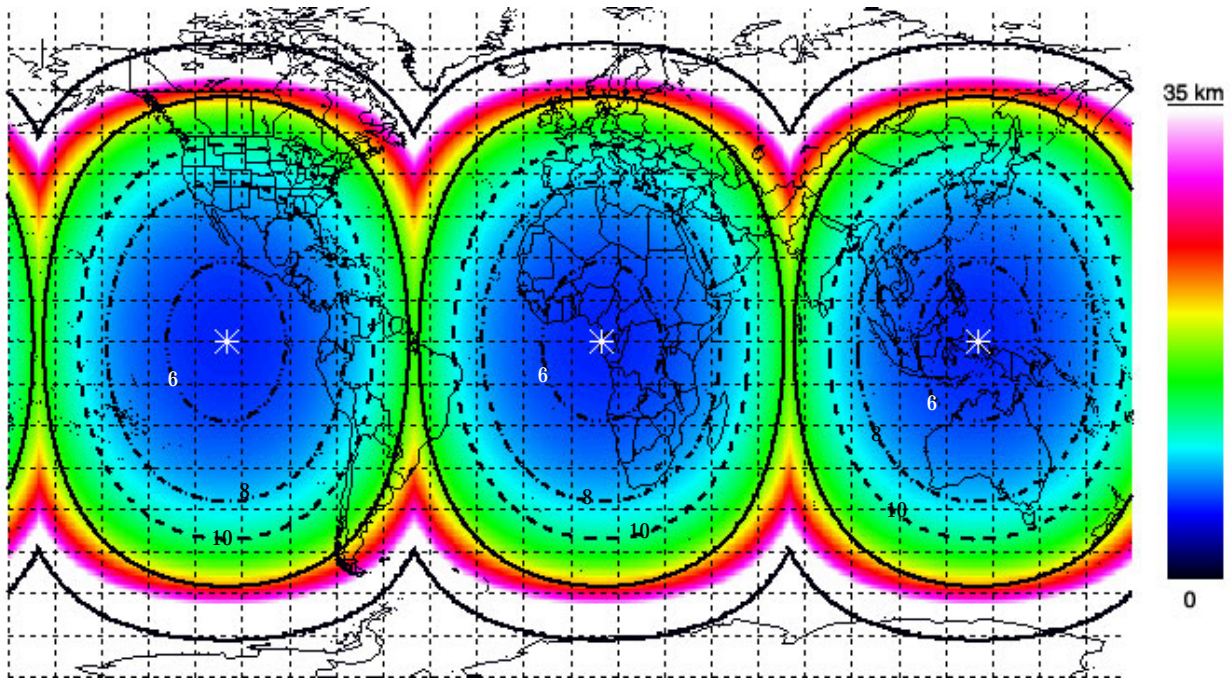


Figure 4-3. Constellation of Three Satellites Located at 10°W, 130°W, and 250°W.

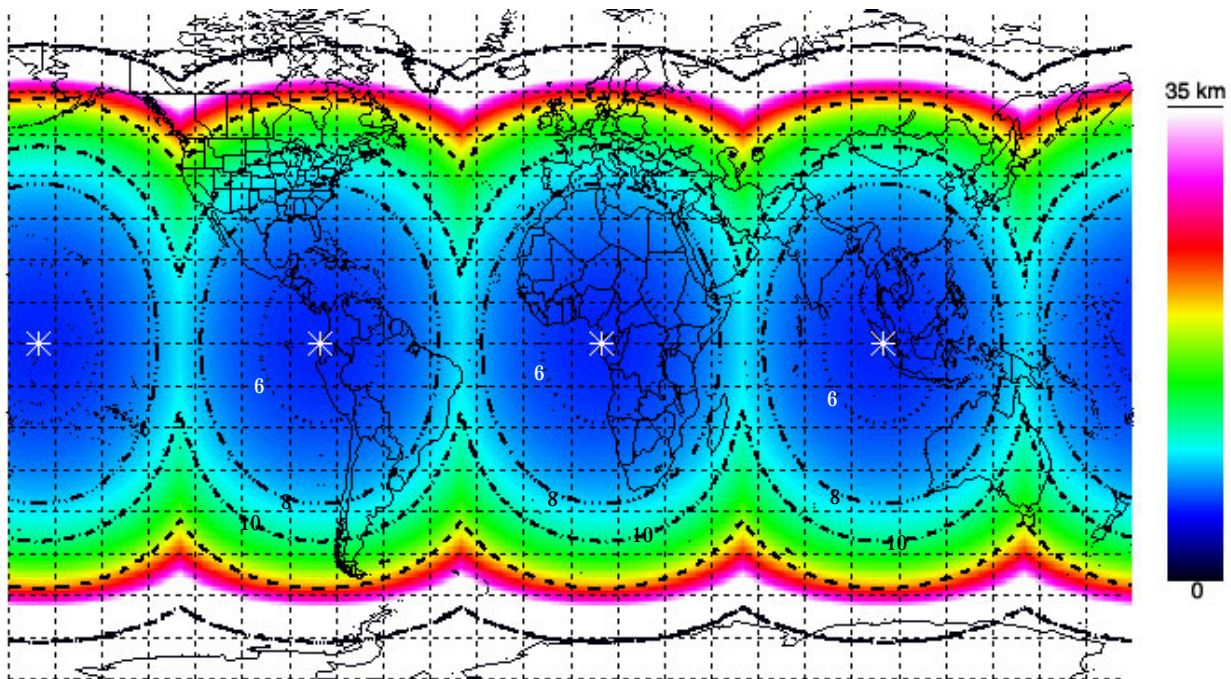


Figure 4-4. Constellation of Four Satellites Located at 10°W, 100°W, 190°W, and 280°W.

4.1.3 Downlink

A trade study was performed to determine the advantages and disadvantages of providing a dedicated instrument X-band downlink system versus utilizing the comsat's downlink resources. The study identified overwhelming schedule and

technical advantages to utilizing the comsat resources. Supplying a dedicated downlink system would require the procurement of an X-band transmitter, obtaining a frequency authorization license, designing and implementing a dedicated ground receiver system, and providing significant engineering effort to design, implement, and test the systems. The lead-time of these items risks the delivery of the secondary payload to the comsat in time for integration and test. The technical advantages of leasing a comsat transponder are numerous for both the flight instrument and the ground system. The instrument-to-comsat interface for downlink of instrument data is not complex, sufficient link margin exists to accommodate the instrument data rate, and there is no need to apply for a frequency authorization license when the payload leases an authorized transponder. The ground system is greatly simplified. With the design of simple ground receiver electronics to look for the instrument data signal instead of the comsat video signal, and with the procurement of a commercial satellite television receiver (for approximately \$200) to provide the RF interface, the ground data receiver is complete and can operate autonomously 24 hours per day. Finally, depending on the business arrangement made for leasing comsat downlink services, and accounting for the cost savings from the simplified instrument, ground system, and operations, cost is not necessarily a disadvantage.

4.1.4 Command and Control

A trade study was performed to determine the advantages and disadvantages of providing a dedicated instrument uplink system versus utilizing the comsat's uplink resources. The study identified overwhelming schedule, cost, and technical advantages to utilizing the comsat resources. Capability for excessive commanding is required in the design of the instrument for testing and on-orbit checkout purposes, but the highly autonomous design of the instrument allows for minimal commanding during the life of the mission. The comsat operators command the comsat on a regularly scheduled basis, and including a small number of instrument commands is of minimal technical and cost impact to the satellite operations. The instrument-to-comsat command interface is a simple, standard, serial interface which is straightforward to design, build, test, and integrate. It is also much cheaper to implement than a dedicated command interface. Supplying a dedicated uplink system would require the procurement of an RF receiver, obtaining a frequency authorization license, designing and implementing a dedicated ground transmitter system, and providing significant engineering effort to design and implement the systems.

Another potential option (for both command uplink and data downlink) is to utilize resources on other communications satellites (e.g. TDRS) to serve as a relay station. Preliminary link analysis has shown that it is possible, with unknown cost, to utilize a TDRS satellite currently in geostationary orbit as a relay station for a secondary payload located on the nadir face of a comsat also located in geostationary orbit. The constraining item, as shown in Figure 4-5, is the 22.5° RF East/West viewing capability of TDRS. The viewing capability was designed for Earth coverage, and thus only allows for TDRS to be used to relay data from other satellites in LEO and certain geostationary orbits that are located on the order of 66,000 km away. Assuming the

visible orbital positions are desirable from a scientific measurement perspective, the RF link analysis has shown that this large distance requires a constraining amount of power for acceptable data relay reliability. This option becomes more feasible and attractive once the next generation of TDRS satellites is operational. Advanced TDRS will have greatly expanded (77°) East/West viewing capability. Thus the relay distance is greatly reduced, and correspondingly, so is the required power. However, for this option there is still the need to provide dedicated communications hardware on the instrument for uplink and/or downlink. This cost would need to be compared with the currently unknown cost of using the advanced TDRS relay communications to determine if the option is worthwhile.

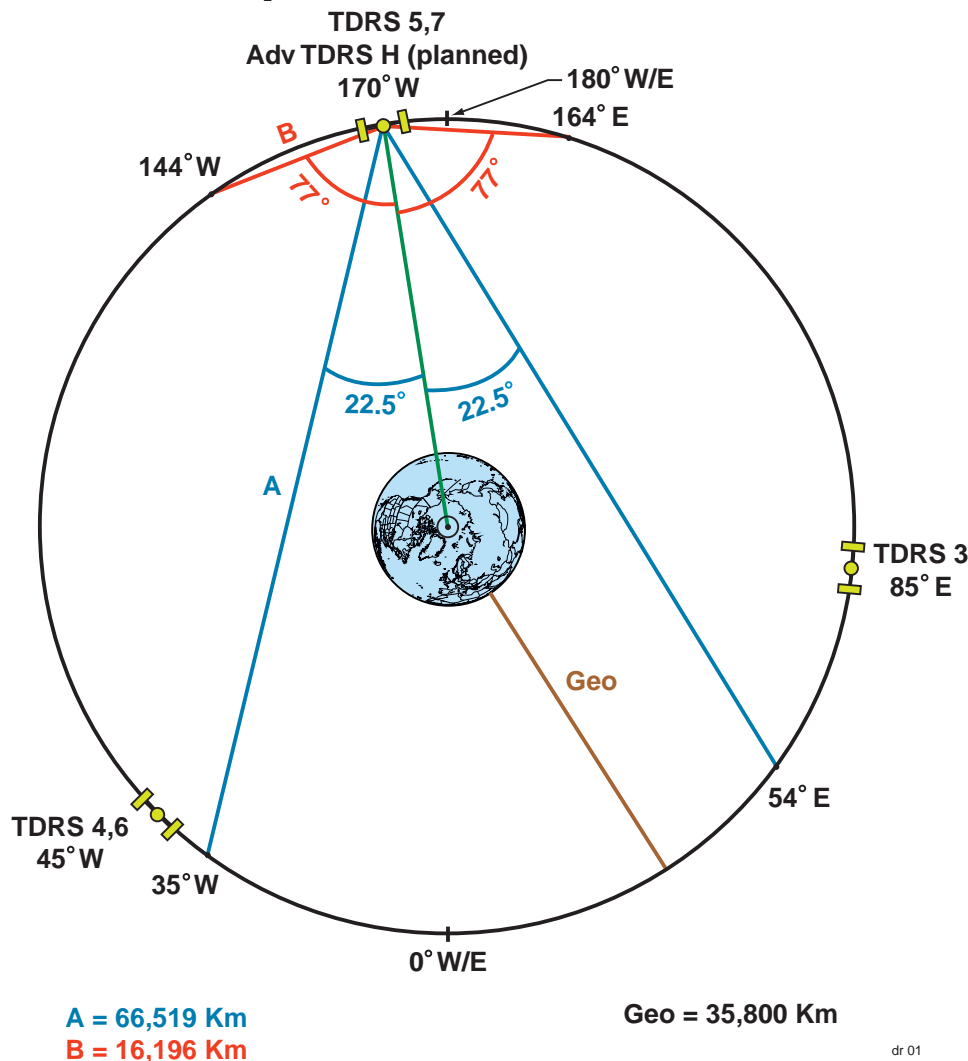


Figure 4-5. TDRS Command and Control Option

4.2 Instrument Trades

This section provides a description of the major trade studies performed to arrive at the baseline instrument. Table 4-2 summarizes the major instrument system trades.

Table 4-2. Instrument Trades

Instrument Subsystem	Trade
IC	Backplane Architecture vs. Stand Alone SBC
	Mongoose V CPU vs. RAD6000 CPU
	Power
CO Sensor	IR FPA selection
	Wavelength
	Single Vs Dual Integration
	Gas Cell Length
Ozone Sensor	Wavelengths, Number of Channels
	UV CCD Selection

4.2.1 Backplane Architecture vs. Stand-Alone Single Board Computer

A trade study was performed to determine the advantages and disadvantages of utilizing a backplane architecture versus a stand-alone single board computer (SBC). The study identified advantages and disadvantages to utilizing both. It concluded that the instrument form factor required by the satellite is the driving consideration. If the form factor allows for a backplane architecture to be implemented, then the IC design, integration, and test are simplified. More importantly, software development may begin immediately on a commercially available development platform that is equivalent in form factor, function, and timing to the flight IC SBC. The disadvantages of this implementation are more mass, volume, and power. However, the IC hardware and software schedule risk is so sufficiently reduced that the backplane approach is still the more attractive option.

4.2.2 Mongoose V CPU vs. RAD6000 CPU

A trade study was performed to determine the advantages and disadvantages of utilizing a Mongoose V (M5) central processing unit (CPU) versus a RAD6000 CPU. The study is tied into the backplane architecture study. Currently the RAD6000 is only available as a commercially produced SBC with a VME backplane. Design with a Compact PCI (CPCI) backplane is ongoing. The M5 is available as a chip, and designs exist and have been built for a stand-alone SBC with the M5. However, the M5 SBCs are not marketed as commercially available products. There are also software development and growth considerations. The RAD6000 is a very similar architecture to the PowerPC CPU, and thus a well-supported set of software development tools with several vendors to choose from is currently, and will continue to be, available. There is no commercially produced version of the M5, and software development is currently performed on a custom built platform. The conclusion is that if the instrument form factor allows for a backplane architecture to be implemented, then the RAD6000 CPU and development process is the preferred choice. If a backplane architecture is not possible, then the M5 CPU and development process is preferred.

4.2.3 Power

A trade study was performed to determine the advantages and disadvantages of building instrument power conversion and distribution inside the instrument or outside the instrument using satellite distribution architecture. The study identified overwhelming schedule and technical advantages to having the comsat provide this outside the instrument, with no significant cost disadvantage. The primary advantage is that the comsat provider has already designed power converters and distribution systems, which are tailored to comsat subsystems. They have already procured long lead item parts, and building one more during their production run for the instrument is of minimal cost and schedule consequence. The instrument development and test schedule is greatly reduced since only commercially available laboratory grade power supplies are required throughout the development. Also, locating this function outside of the instrument also helps to minimize the electro-magnetic interference (EMI) concerns that routinely cause project schedule delays by addressing EMI issues during the comsat design (well before the instrument is delivered).

4.2.4 IR FPA Selection

A survey of currently available FPAs and detectors was conducted. The survey encompassed a wide range of detector materials and manufacturers. The survey is presented in Appendix A. Instrument models were developed to perform trade studies of the FPAs, select a target FPA, and determine the expected overall instrument performance. The FPA parameters are the most variable parameters used in the model. The FPA parameters are a function of operating temperature and configuration.

4.2.4.1 Instrument Model

Excel and Mathcad were used to develop an instrument model. The primary model parameters are shown in Table 4-3. The first section of the instrument model converts the top of the atmosphere radiances into the photon flux collected by the optical system in a single pixel. The throughput factor ($A\Omega$) is a function of the solid angle subtended by a single pixel and the aperture of the optical system. The throughput factor is given by equation 1.

$$A\Omega = \pi \cdot \left(\frac{EPD}{2} \right)^2 \cdot IFOV^2 = 1.155 \times 10^{-7} \text{ cm}^2 \cdot \text{sr} \quad (1)$$

Where, EPD is the entrance pupil diameter = 25 mm, and IFOV is the instantaneous field of view = 153 μ radians. The photon flux per pixel is calculated using equation 2.

$$\text{photon flux} = \text{radiance} \cdot A\Omega \cdot \frac{\lambda}{h \cdot c} \quad (2)$$

Where the *radiance* is the value calculated at the top of the atmosphere using MODTRAN, λ is the wavelength of incident radiation, h is Planck's constant, and c is the speed of light. The rate of electrons generated by the incident photon flux is given by equation 3.

$$\text{electrons} = (\text{photon flux}) \cdot \eta \cdot \tau_{\text{optics}} \cdot \tau_{\text{filter}} \quad (3)$$

Where, η is the quantum efficiency, τ_{optics} is the optical system transmission, and τ_{filter} is the filter transmission. The integration time desired is the time that will maximize the use of the full well without saturating any pixels. In this case the desired fraction of full well to be utilized is 80% in order to provide some engineering margin. The integration time is calculated using equation 4.

$$t_{int} = \frac{0.8 \cdot W}{(\max electrons) + I_{leak}} \quad (4)$$

W is the full well depth, $\max electrons$ are the maximum rate of electronics generated by the incident radiation, and I_{leak} is the dark current rate. The signal-to-noise is defined as the number of signal electrons divided by the number of noise electrons. The noise electrons are a function of the read out noise, the dark current and shot noise and are given by equation 5. The signal electrons are the electron rate multiplied by the integration time.

$$N_{rms} = \sqrt{N_{read}^2 + electrons \cdot t_{int} + I_{leak} \cdot t_{int}} \quad (5)$$

where, N_{read} is the number of read out electrons. Thus the single frame signal-to-noise ratio is given by equation 6.

$$SNR_1 = \frac{electrons \cdot t_{int}}{N_{rms}} \quad (6)$$

SNR_1 is the single frame signal-to-noise ratio. The required number of images is given by equation 7.

$$\# images = \left(\frac{SNR_{req}}{SNR_1} \right)^2 \quad (7)$$

SNR_{req} is the required signal-to-noise ratio.

4.2.4.2 Trade Studies

The scene radiances and dynamic range vary with the viewing geometry (solar zenith angle and look angle) as well as the surface composition. The dynamic range affects the performance since the integration time is determined by the maximum radiance and the signal-to-noise ratio is limited by the minimum radiance. The instrument model has been used to determine the operating parameters as a function of the scene variations. The instrument model has been used to calculate the effect of parameter changes on the overall operational time line.

4.2.4.2.1 Dark Current

The dark current affects the instrument performance and is tied to the FPA operating temperature and material selection. Figure 4-6 shows the effect of dark current on the observation parameters. With high levels of dark current the observation time quickly becomes unreasonable.

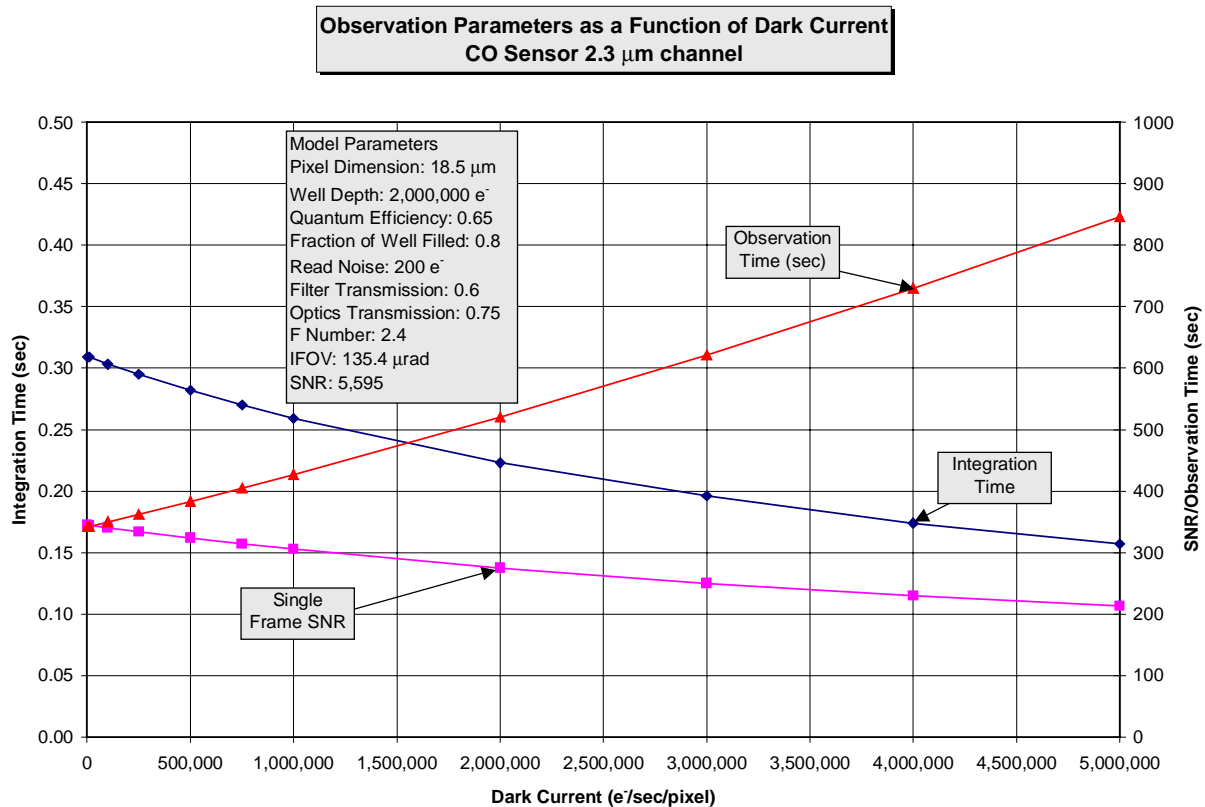


Figure 4-6. CO Sensor Observation Parameters as a Function of Dark Current

4.2.4.2.2 Well Depth

The well depth is one of the more important parameters. Figure 4-7 shows that the well depth dramatically affects the observation time. Currently available focal plane arrays have well depths of 3-4 million electrons and can be increased by a factor of 2 with a change to a ripple mode multiplexor.

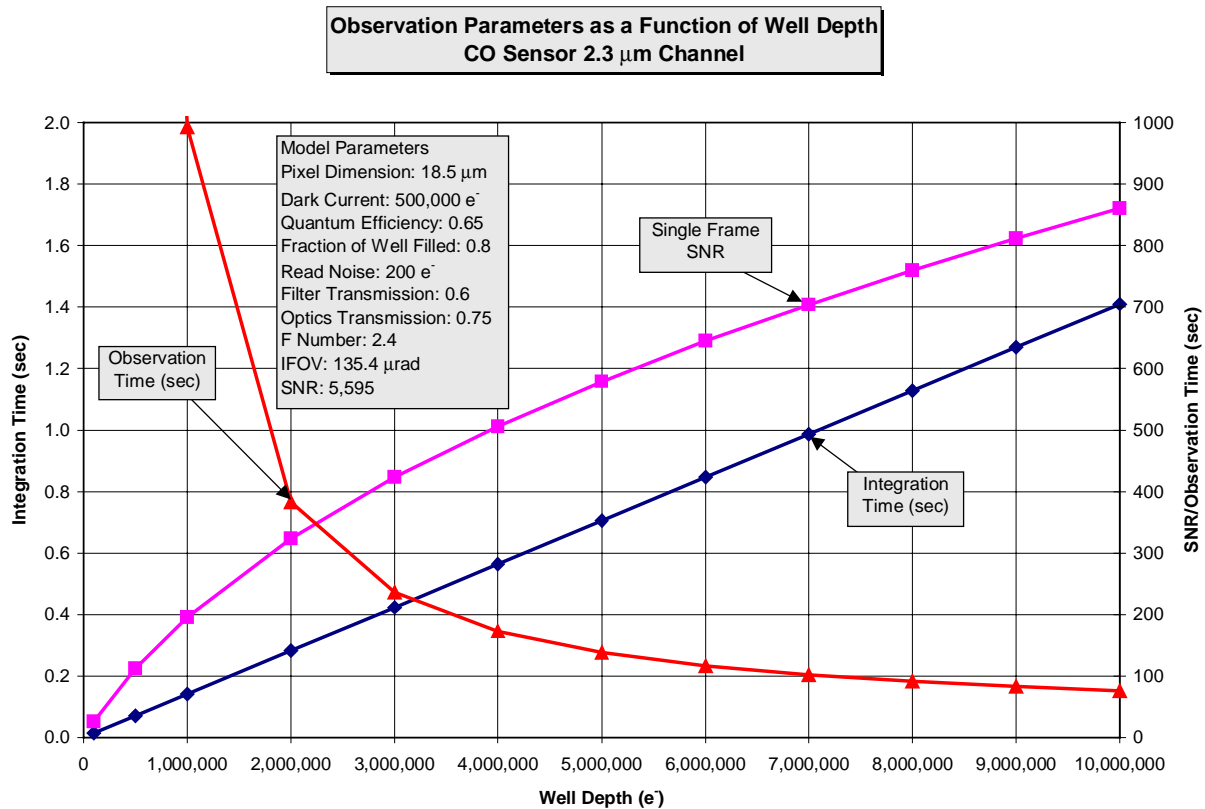


Figure 4-7. CO Sensor Observation Parameters as a Function of Well Depth

4.2.4.2.3 Transmission

The filter or optical transmission also affects the integration and observation times. As one would surmise, higher transmission leads to shorter integration and observation times. Other parameters, such as quantum efficiency have similar effects on the instrument performance.

4.2.4.2.4 Signal-to-Noise Ratio

The required signal-to-noise ratio has a direct impact on the time required to acquire the measurement. An increase in the required signal-to-noise ratio increases the number of images required and the total observation time.

4.2.5 CO Sensor Wavelengths

We evaluated two spectral regions for CO measurements: the fundamental band at 4.67 μm and the first overtone band at 2.3 μm . We selected a dual band system for our design.

The 4.67 μm band was used by the MAPS experiment, which flew aboard the Space Shuttle in 1981, 1984, and twice in 1994. These CO measurements at 4.67 μm are based on thermal emission, which is available day and night. Because the

measurements were obtained in low Earth orbit, several days of data acquisition were required to form a single, composite, near-global distribution of CO. The composite data provide the abundance of CO time averaged over a Space Shuttle mission (10-14 days) on a global grid (100 x 100 km at the equator). In addition, the MAPS data provide indications of long range transport 24 hours a day. At 4.67 μm , N₂O is the reference gas for the correlation measurement, used to identify clouds in the scenes and enhances data retrieval.

At 2.3 μm , thermal emission from the planet is negligible, and the measurement is based on reflected sunlight. Consequently, the analyses in this report consider CO lines in the incident sunlight (“solar CO lines”) as well as the atmospheric CO lines. Methane is the reference gas for the correlation measurement, used to identify the presence of clouds in each pixel. The spectroscopy of methane has improved considerably over the last decade, and we have used the most current spectral databases. At 2.3 μm , the measurement is sensitive to the surface, and therefore to local sources and sinks. At 4.67 μm , the measurement is most sensitive in the middle troposphere. Present 2.3 μm FPA technology permits rapid acquisition of data (milliseconds per sample), and geostationary orbit permits continuous viewing of the Earth, enabling frequent measurements, and identifying atmospheric processes with very short (~hourly) characteristic times. We have designed the CO sensor to operate at 2.3 and 4.67 μm .

4.2.6 Single Vs Dual Integration

The dual integration sequence has two integration times: one for the low radiance portion of the scene (water), and one for the high radiance of the scene (land). Splitting the scene in two allows for the half scene dynamic range to be reduced by the square root of the full scene dynamic range. This allows for a significant reduction in the number of frames and time required in order to meet the 5,600:1 signal to noise ratio. Table 4-3 contains the parameters used to calculate the time required to acquire a full series of images for the two cases. There may also be a relaxation of the pointing requirements for the low radiance portion of the scene over the ocean, where there are no sources of CO. The required dynamic range determines how long integration can last before filling the well, while the minimum radiance determines the signal to noise ratio since the system is nominally background limited. Thus a reduction in the dynamic range greatly increases the allowable integration time and increases the minimum fraction of the well filled and signal to noise ratio, which reduces the number of frames required.

Table 4-3. Parameters Used for Single Vs Dual Integration Comparison

Detector Model Parameters			
Value	Units	Variable	Description
2.3474	μm	λ	Center Wavelength
0.0652	μm	$\Delta\lambda$	Wavelength Range
35,800	km	z	Altitude

Detector Model Parameters			
Value	Units	Variable	Description
10.98	km	FP	Nadir Footprint
25	mm	EPD	Entrance Pupil Diameter
0.02	-	α	Albedo
185	-	D	Scene Dynamic Range
13.6	-	d	Dynamic Range of Split Scene
200	e ⁻	N _{readout}	FPA Readout Noise
0.65	e ⁻ /photon	η	Quantum Efficiency
0.8	-	W _{frac}	Fraction of FPA Well Filled
0.033	sec	t _{readout}	Readout Time
0.005	sec	t _{dead}	Dead Time, No Integration and No Readout
0.60	-	τ_{filter}	Interference Filter Transmission
0.75	-	τ_{optics}	Optics Transmission
5,600	-	SNR _{req}	Required Signal to Noise Ratio
2,000,000	e ⁻	w	Well Depth

The results of the calculations are summarized in Table 4-4. The comparison of the single and dual integration approaches shows that the total time to acquire a full disk image with the required signal to noise is significantly reduced with the dual integration approach.

Table 4-4. Summary of Single/Dual Integration Comparison Results

Parameter	Single Integration Time	Dual Integration Time
Minimum Signal to Noise Ratio (single frame)	41	344
Integration Time	0.006 sec	0.077 sec, 0.006 sec
Wheel Rotation Rate	1.68 Hz	1.68 Hz
Number of Frames	18,600	265
Total Observation Time	184 min	7.2 min

4.2.7 Gas Cell Length

A trade study has been performed to determine the length of the correlation gas cell. The signal to noise ratio (SNR) depends on instrument parameters, state of the atmosphere, and condition of observation. Figure 4-8 shows the effect of the cell length on the required signal to noise ratio. This figure indicates that the optimal cell length is approximately 8 cm, which corresponds to a SNR of 5,600.

Required Signal to Noise Ratio
as a Function of Cell Length
(p = 1,000 mb)

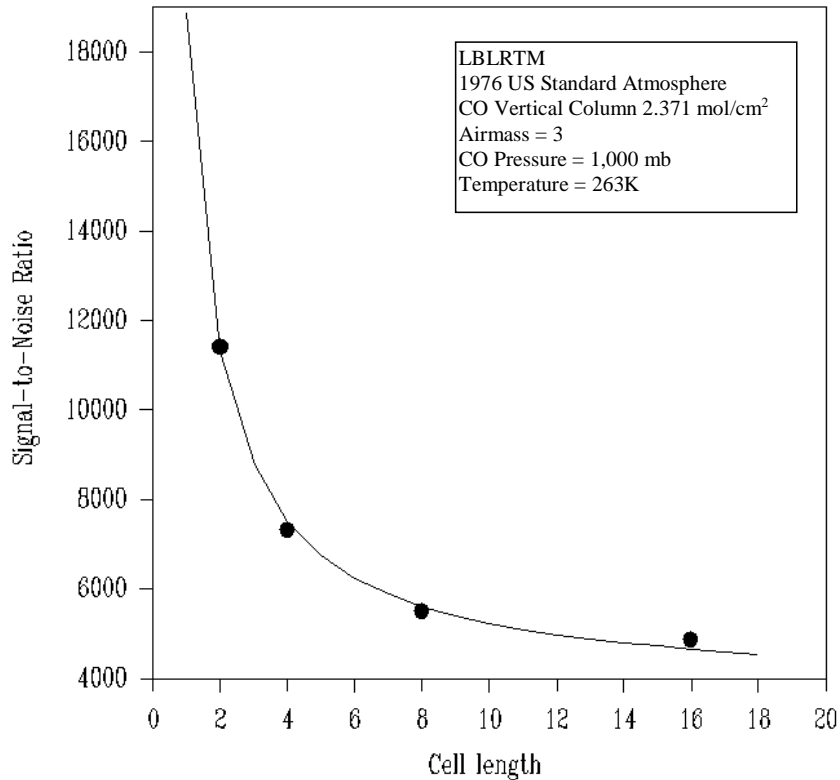


Figure 4-8. Required Signal to Noise Ratio as a Function of Cell Length

4.2.8 Ozone Sensor Wavelengths

Interference filters located on a rotating filter wheel define the ozone sensor channels. The current measurement concept utilizes 12 channels as shown in Table 3-1. The channel selections provide for a measurement suite to perform important atmospheric chemistry measurements. The utilization of a filter wheel allows for the increase or decrease in the number of channels without a major impact on the instrument design. The channels required for the accurate measurement of ozone are derived from the TOMS and SBUV/2 instruments.

4.2.9 UV CCD Selection

A survey of currently available CCDs was conducted. The survey encompassed a wide range of manufacturers and is presented in Appendix B. An instrument model was developed to guide the selection of the CCD array. The CCD parameters are the most variable parameters used in the model. The CCD parameters are a function of operating temperature and configuration. The dark current is a function of both the configuration (MPP or Non-MPP) and temperature. The read noise is a function of the bandwidth of the electronics system. Reducing the required electronics bandwidth by

increasing the number of amplifiers that are used can minimize the read noise. The system is designed to be used without a mechanical shutter. The shuttering mechanism is a fast transfer from the active area to a storage area. The array is actually 2048x1024 with half of the array masked off and used as the storage area. This transfer time affects the well depth and is also a function of the MPP mode used. In general the faster transfer time leads to less image blurring, or contamination of the image as the array is transferred across the array to the storage area. There are two transfer configurations available: 1) full frame transfer, 2) split frame transfer. Each storage section requires an amplifier. Thus the allowable amplifier configurations are a function of the frame transfer mode specified. The split frame array can have either 2 or 4 amplifiers, while the full frame array can have 1, 2, or 4 amplifiers. The number of amplifiers used also affects the bandwidth of the electronics, the thermal characteristics of the CCD socket board, and the number of electronics components. The CCD parameters are shown for two cases, MPP mode, and non-MPP mode, in Table 4-5.

Table 4-5. CCD Parameters

CCD Parameters	
Pixel Dimension	12 μm
Number of Pixels	1024x1024
Electronics Bandwidth	1 MHz
Read Noise (1 MHz BW)	10 e^-
Fraction of Well Filled	0.8
Quantum Efficiency	0.45
MPP Well Depth	85,000 e^-
MPP Dark Current	20-50 pa/cm^2
MPP Fast Frame Transfer Time	8 $\mu\text{s}/\text{row}$
Non-MPP Well Depth	240,000 e^-
Non-MPP Dark Current	350 pa/cm^2
Non-MPP Fast Frame Transfer Time	12 $\mu\text{s}/\text{row}$

The dark current is a function of temperature as well as the MPP or non-MPP mode in Table 4-6. The main benefit of MPP mode is the reduced dark current. The dark current values in this table were read off the standard SITE dark current Vs temperature graph.

Table 4-6. Dark Current as a Function of Temperature

Dark Current as a Function of Temperature		
Temperature ($^{\circ}\text{C}$)	MPP Mode (e^-)	Non-MPP Mode (e^-)
30	750	7,500
20	375	2,500
10	150	1,000
0	50	125

Dark Current as a Function of Temperature		
Temperature (°C)	MPP Mode (e)	Non-MPP Mode (e)
-10	20	38
-20	6.25	12.5
-30	2	2.5
-40	0.25	0.5
-50	0.1	0.2

4.2.9.1 Instrument Model

The first section of the instrument model converts the top of the atmosphere radiances into the photon flux collected by the optical system in a single pixel. The throughput factor ($A\Omega$) is a function of the solid angle subtended by a single pixel and the aperture of the optical system. The throughput factor is given by equation 9.

$$A\Omega = \pi \cdot \left(\frac{EPD}{2} \right)^2 \cdot IFOV^2 = 3.142 \times 10^{-8} \text{ cm}^2 \cdot \text{sr} \quad (9)$$

Where, EPD is the entrance pupil diameter = 8.76 mm, and IFOV is the instantaneous field of view = 153.4 μ radians. The photon flux per pixel is calculated using equation 10.

$$\text{photon flux} = \text{radiance} \cdot A\Omega \cdot \frac{\lambda}{h \cdot c} \quad (10)$$

Where the *radiance* is the value calculated at the top of the atmosphere using MODTRAN, λ is the wavelength of incident radiation, h is Planck's constant, and c is the speed of light. The rate of electrons generated by the incident photon flux is given by equation 11.

$$\text{electrons} = (\text{photon flux}) \cdot \eta \cdot \tau_{\text{optics}} \cdot \tau_{\text{filter}} \quad (11)$$

Where, η is the quantum efficiency, τ_{optics} is the optical system transmission, and τ_{filter} is the filter transmission. The integration time desired is the time that will maximize the use of the full well without saturating any pixels. In this case the desired fraction of full well to be utilized is 80% in order to provide some engineering margin. The integration time is calculated using equation 12.

$$t_{\text{int}} = \frac{0.8 \cdot W}{(\text{max electrons}) + I_{\text{leak}}} \quad (12)$$

W is the full well depth, *max electrons* are the maximum rate of electronics generated by the incident radiation, and I_{leak} is the dark current rate. The signal-to-noise is defined as the number of signal electrons divided by the number of noise electrons. The noise electrons are a function of the read out noise, the dark current and shot noise and are given by equation 13. The signal electrons are the electron rate multiplied by the integration time.

$$\text{Nrms} = \sqrt{N_{\text{read}}^2 + \text{electrons} \cdot t_{\text{int}} + I_{\text{leak}} \cdot t_{\text{int}}} \quad (13)$$

where, N_{read} is the number of read out electrons. Thus the single frame signal-to-noise ratio is given by equation 14.

$$SNR_1 = \frac{electrons \cdot t_{int}}{N_{rms}} \quad (14)$$

SNR_1 is the single frame signal-to-noise ratio. The required number of images is given by equation 15.

$$\#images = \left(\frac{SNR_{req}}{SNR_1} \right)^2 \quad (15)$$

SNR_{req} is the required signal-to-noise ratio.

4.2.9.2 Trade Studies

The scene radiances and dynamic range vary with wavelength. The dynamic range affects the performance since the integration time is determined by the maximum radiance and the signal-to-noise ratio is limited by the minimum radiance. The instrument model has been used to determine the operating parameters as a function of the channel differences. In addition the CCD performance varies with temperature and specifications. The instrument model has been used to calculate the effect of parameter changes on the overall operational time line.

4.2.9.2.1 Dark Current

The first parameter examined is the dark current. The dark current is highly dependent on the CCD operating temperature and also depends on the specified operating mode. Figure 4-9 shows the effect of dark current changes on the integration time, the single frame signal-to-noise ratio, and the channel observation time to meet the 250:1 signal-to-noise goal. Note that the plots show dark currents at the end of life and are much higher than are expected at the beginning of life. The primary difference between the MPP and non-MPP operation is that the well depth is larger for the non-MPP mode. The operating temperature to produce the same level of dark current is lower for non-MPP operation. This figure indicates the need to cool the CCD array to minimize the dark current.

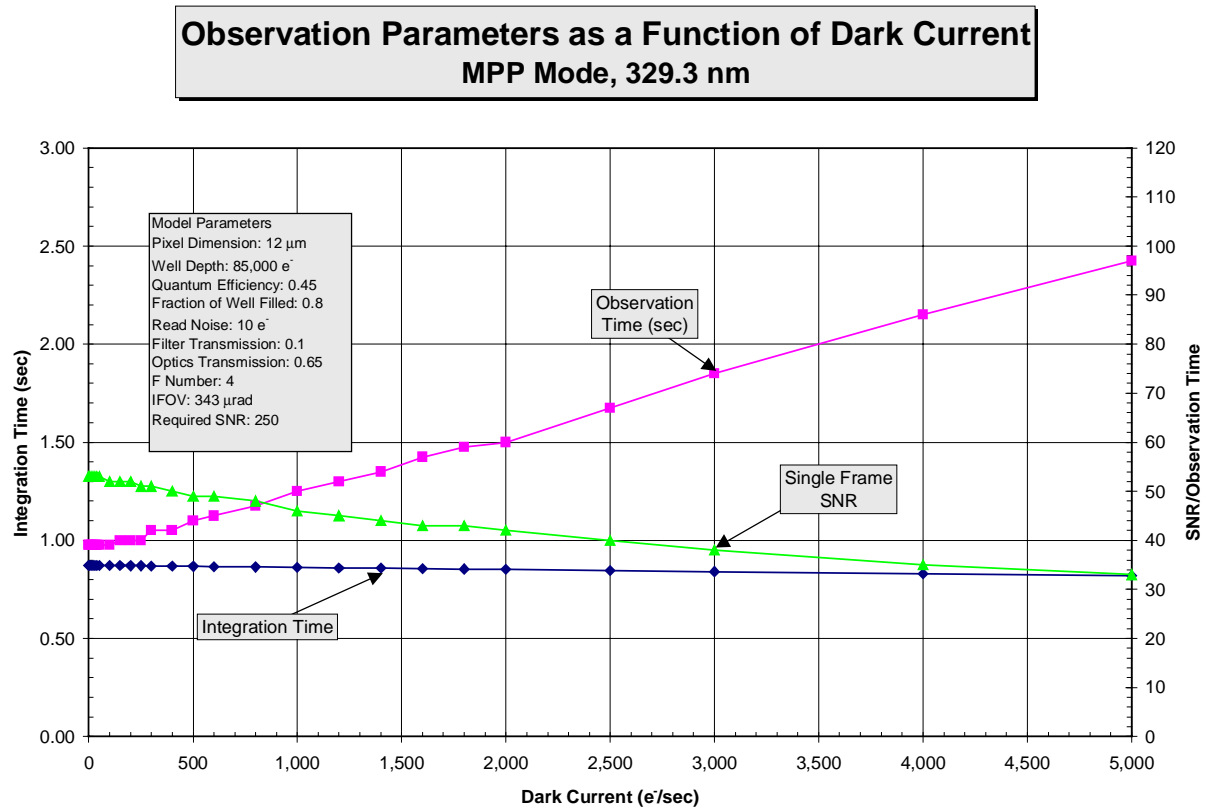


Figure 4-9. Ozone Sensor Observation Parameters as a Function of Dark Current

4.2.9.2.2 F/Number

The selection of the optical system F/number has a large impact on the system performance. The F/number determine how much light is collected and as would be expected the observation time is strongly dependent on the F/number. The F/number also affects the integration time. This is due to two factors: 1) the reduced photon flux with increasing F/number, and 2) the increased number of dark current electrons with the decreased photon flux associated with the increased F/number. The F/number also has an effect on the performance of the interference filters, which is not addressed in this system study.

4.2.9.2.3 Well Depth

The well depth, or the number of electrons that can be collected before saturation, also directly affects the integration and total observation times. The integration time increases linearly with increasing well depth. The total observation time decreases with increasing well depth.

4.2.9.2.4 Filter (or Optical) Transmission

The filter or optical transmission also affects the integration and observation times. As one would surmise, higher transmission leads to shorter integration and

observation times. Other parameters, such as quantum efficiency have similar effects on the instrument performance.

4.2.9.2.5 Comparison of MPP and Non-MPP Modes

As previously mentioned the primary differences between MPP and non-MPP mode are the well depth and the dark current. The impact of these differences is shown in for one wavelength in Figure 4-10. This figure shows the integration time, single frame signal-to-noise ratio, and the observation time for both modes and for each channel as a function of the CCD array operating temperature. There are several important features illustrated by this figure: 1) the low temperature performance (i.e. less than 250K) for both MPP and non-MPP are comparable, and 2) the non-MPP mode of operation degrades much more rapidly than the MPP mode with increasing temperature.

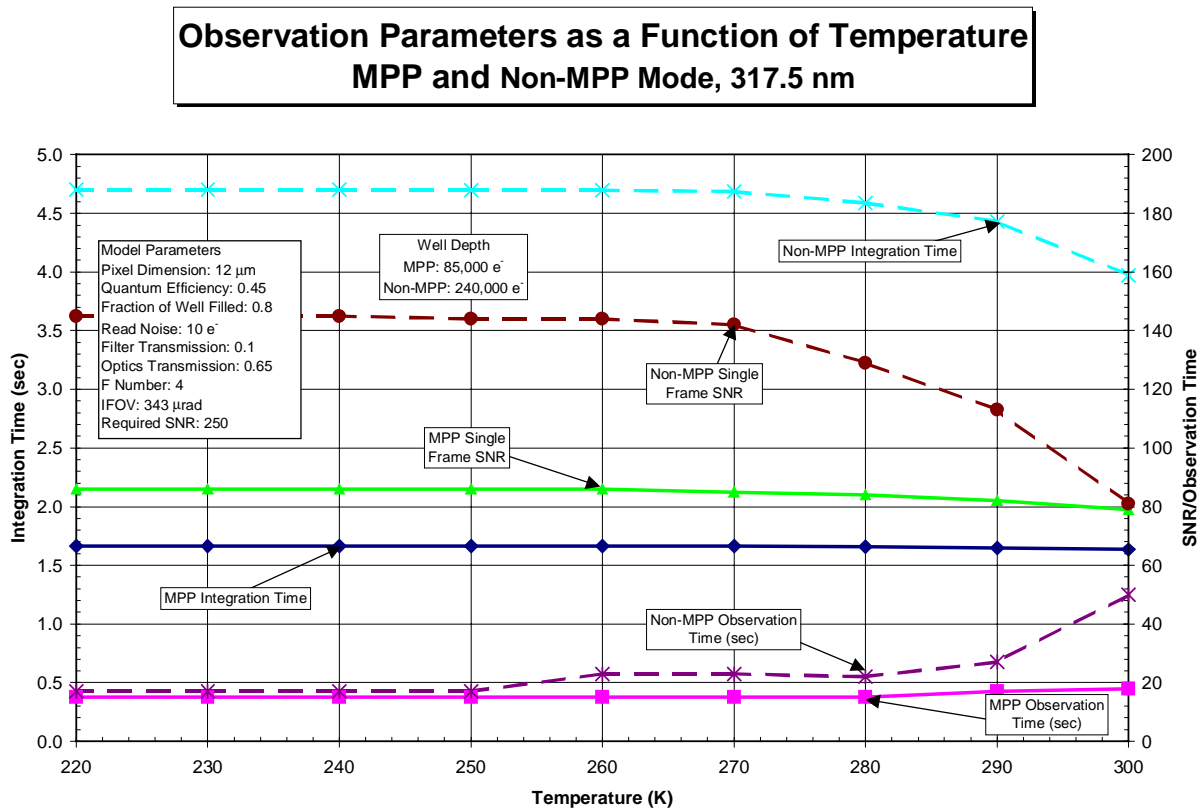


Figure 4-10. Comparison of Ozone Sensor Observation Parameters as a Function of Temperature.

Figure 4-11 shows the observation time as a function of CCD array temperature for the four channels and both modes. One of the main features shown in this log figure is that channel 2 requires significantly more time to meet the signal-to-noise ratio requirements than the other three channels. This is due to the larger scene dynamic range at the 322.3 nm band. This large difference in the scene dynamic range may be an artifact of the MODTRAN 3 radiance calculations, but it serves to illustrate the effect

of the scene dynamic range on the observation time. It shows just how quickly the time required to make the measurement becomes unreasonable and violates the desired 15-minute interval between measurements. Figure 4-12 displays the same information however since it is not a log plot it emphasizes the effects of the operating temperature in the other three channels.

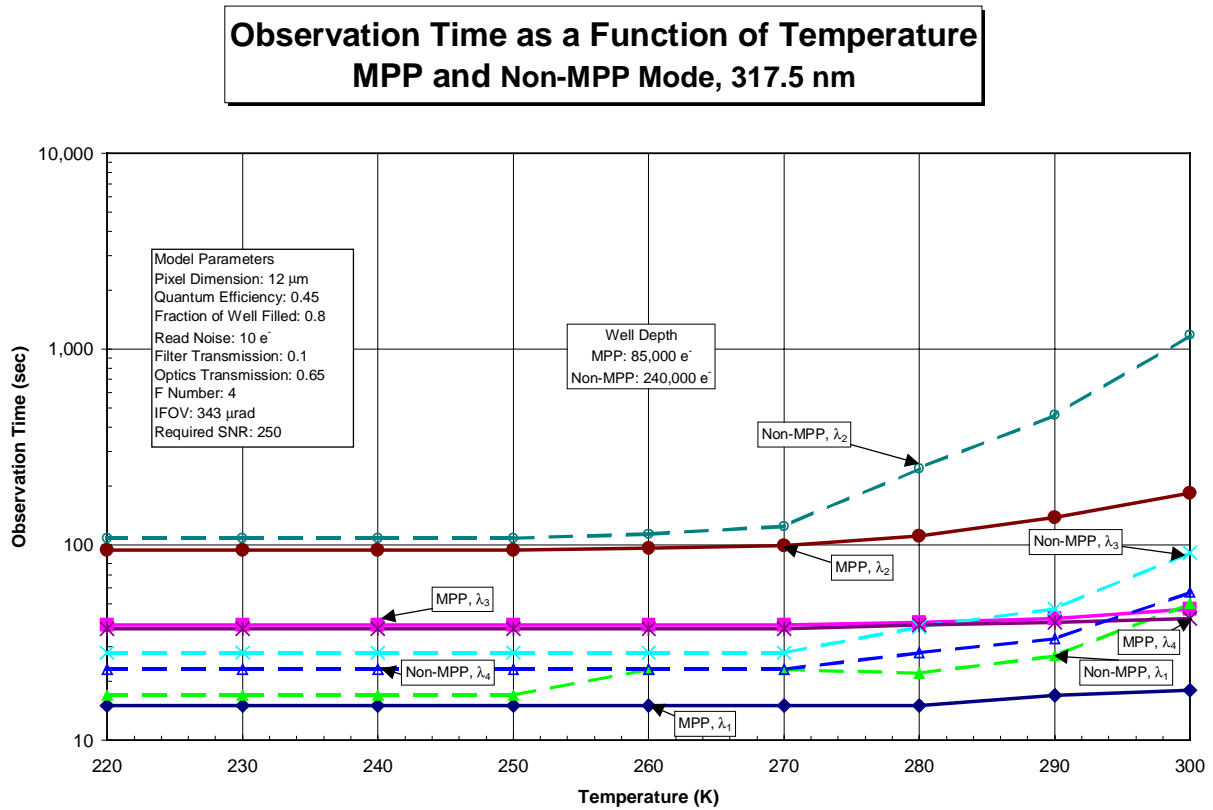


Figure 4-11. Comparison of Ozone Sensor Observation Time as a Function of Temperature (log scale)

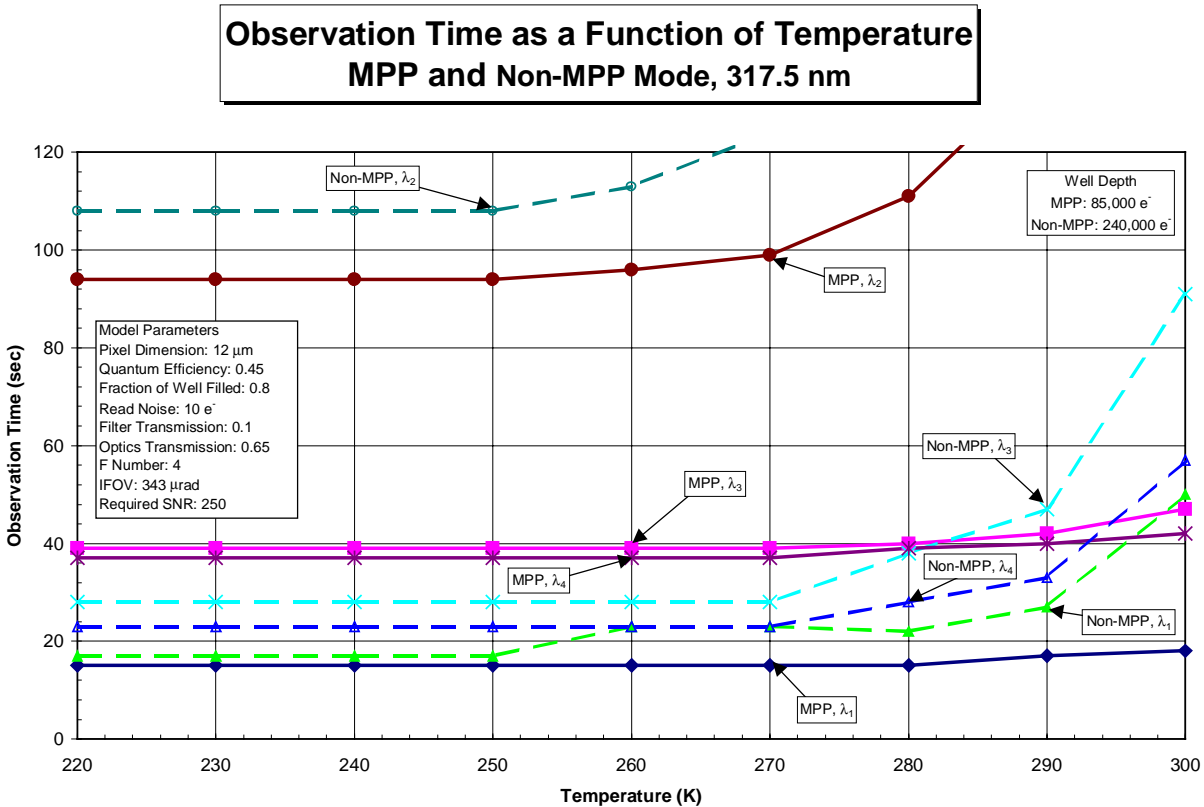


Figure 4-12. Comparison of Ozone Sensor Observation Time as a Function of Temperature

4.2.9.2.6 Signal-to-Noise Ratio

The required signal-to-noise ratio has a direct impact on the time required to acquire the measurement. An increase in the required signal-to-noise ratio increases the number of images required and the total observation time.

4.2.9.2.7 Tri-State Clocking

Tri-state clocking incorporates the best of the MPP and non-MPP modes. It uses the MPP mode clocking to integrate, performs the fast frame transfer using non-MPP mode clocking, and uses MPP mode for the storage region and readout. This allows for the use of the low dark current mode for integration and storage while using the fast frame transfer capability of the non-MPP mode.

4.2.9.2.8 Fast Frame Transfer Time

The Pluto CCD array is actually 2048x1024, where half of the array is active and the other half of the array is storage. The storage section of the array is used to stop the integration and store the collected charge while it is being read out. The active area is always collecting photons. The time that it takes to transfer charge from the active area to the storage area is the fast transfer time. The fast transfer time is significant because charge is collected as the signal is transferred to the storage region, which results in

smearing of the image. It is important to keep the time required for the fast transfer significantly shorter than the integration time in order to keep the smearing to an acceptable level. The fast transfer time is a function of the mode (MPP or non-MPP) and the well depth and CCD configuration as shown in Table 4-7. The CCD can be set up either as a full frame (i.e. with the storage region at one end) or as a split frame with the storage region split into two sections, one at each end of the array. The split frame has the advantage of reducing the number of rows that must be transferred by two. The table shows that the image smearing is minimized for the shallow non-MPP and the tri-state configurations. The tri-state configuration has superior noise performance and would be the operational mode of choice.

Table 4-7. Fast Frame Transfer Time

Fast Frame Transfer Time					
Mode	Well Depth (e-)	Transfer Time per Row (μ s/row)	Integration Time (sec)	Transfer Time (sec)	Transfer Time Percentage of Integration time
MPP	85,000	8	0.6	0.0041	0.68
Non-MPP	240,000	12	1.8	0.0061	0.34
Non-MPP	85,000	1.2	0.6	0.0006	0.1
Tri-State	85,000	1.2	0.6	0.0006	0.1

5. Technology Assessment

This section discusses the current technology capabilities and the desired technical capabilities. Table 5-1 presents the key technological capabilities for Geo Tropsat.

Table 5-1. Technology Capability Matrix

Technology	Current Capability	Desired Capability
IR FPA	2048x2048 HAWAII (cryo-cooled, slow readout) HgCdTe on Sapphire & 1024x1024 HgCdTe on Si	2048x2048 TE cooled, 10 Hz readout, >25M e ⁻ , low noise, HgCdTe on CdZnTe or HgCdTe on Si
UV CCD	STIS 1024x1024 & Pluto Frame Transfer 1024x1024	2048x2048 Frame Transfer Array with large well
Electronics	Discrete electronics boards	Electronics integrated into the mechanical and thermal structure (multifunctional structures)
Thermal	Composite radiators	Composite multifunctional structure
Software	Unique, unmaintainable, inflexible, implementation dependant sensor system software	Portable, maintainable, dynamically configurable, implantation independent sensor system software

5.1 IR FPA

The FPA is the heart of the sensor and drives the design of the rest of the instrument. The ideal FPA will have a large well, large format (2048x2048), low noise, fast readout, and operate at high temperatures. The current state-of-the-art is a hybrid 1024x1024 HgCdTe on Si manufactured and demonstrated in the lab by Rockwell. This focal plane array design incorporates a snapshot readout with a well capacity of 3.5 Me⁻. The materials used to construct this hybrid array provide lower noise operation, which translates into a higher operating temperature for equivalent noise performance. These arrays have significantly better performance than the HAWAII devices which are currently in wide use by the astronomical community. Rockwell is also building FPAs utilizing CdTe as a substrate that has a noise (dark current) performance approximately three orders of magnitude lower than the HAWAII material. These FPA materials can operate at temperatures 40-50°C higher than the conventional HAWAII FPAs. This increase in operating temperature allows for the FPAs to be easily cooled with radiative coolers simplifying the system design. Demonstrated performance of HgCdTe FPAs on these two advanced substrates and scaling to 2048x2048 devices should be achieved in the near future. This type of FPA technology should be actively pursued since it has many desirable features and will simplify instrument design. These large format focal plane arrays enable compact instruments designed for geostationary orbit by allowing for continuous staring at the scene.

5.2 UV-Visible CCD

CCD technology is fairly mature however advances in format size and noise performance are still being made. The current state of the art is the backside thinned UV enhanced STIS 1024x1024 CCD currently in use on the Hubble Space Telescope, which will be replaced with the next generation, advanced camera system (ACS) on the next Hubble servicing mission. These CCDs are spaceflight qualified and could be used for the Geo Tropsat instrument. However the instrument would be improved with the development of flight qualified 2048x2048 active area frame transfer CCDs. The capability to quickly transfer the charge from an image into the storage area on frame transfer CCDs enable the development of simpler instruments by eliminating the need for a mechanical shutter. Frame transfer arrays with a 1024x1024 active area currently exist but have yet to be demonstrated on orbit.

5.3 Electronics

An approach to improving overall electronics performance is to progress towards the multifunctional structure (integrated electronics in the structure). Since each instrument requires some form of instrument controller (IC), the IC will be used as a basis for discussion. The current state of the art in development for an IC uses the CPCI backplane architecture. This utilizes the industry standard PCI bus architecture in a compact, ruggedized form factor, and is significantly smaller and less power consuming than the currently dominant VME backplane architecture.

The first step to approach the ideal is to reduce the size/volume of the IC by further reducing the backplane architecture, and eventually, eliminating the concept of a backplane altogether. Technology development has been ongoing in this area and has produced some viable initial options, such as Chip On-Board technology. Once the backplane has been eliminated, the next step would be the removal of the IC housing. The IC printed circuit boards (PCBs) would be mounted (e.g. via standoffs) internal to the instrument housing, utilize flexible cabling for circuit connections, and the instrument housing would provide radiation shielding. The next step would be to reduce the number of PCBs in the IC. Options for this include liberal use of multichip modules (MCMs) and application specific integrated circuits (ASICs). Note that this option is currently very expensive for fabricating a low quantity of devices, and this cost can be a limiting factor for many missions. The final step in the evolution to multifunctional structure would be to embed electronics circuitry directly into the spacecraft structure, and the structure itself would be built to provide for radiation shielding and electrical connections for power and data.

Another technology development currently in its early stage is the production of radiation tolerant coatings. Conceptually, these coatings may be applied to PCBs in a manner similar to the application of conformal coating. Different coatings of varying thickness may be applied to protect against the particular types of radiation expected in the target environment. Potential results range from making radiation soft parts acceptable for spaceflight to being able to directly design systems utilizing COTS electronic components.

Multifunctional structures can reduce instrument size and mass by incorporating electronics, thermal management, and radiation shielding into composite structural panels. Mounting electronic parts directly to the surface of the composite panels eliminates electronic boxes and cabling. The electronic parts are interconnected with flexible circuitry embedded in the panel. The composite panels may form the primary load-bearing structure of the spacecraft, and dissipate heat from the electronics. The composition of the composite material can be tailored to provide radiation shielding for the electronics. Mass reductions by factors of 2-3 can be achieved by using highly integrated multifunctional structures in place of conventional structures and electronics boxes. Conformal radiation shielding minimizes the adverse effects of the space radiation environment on the function of instrument electronics. These effects include charging, single event upsets, and part latch-up caused by high-energy protons and electrons. The conformal shielding can be coated over or shaped around a radiation sensitive part. The shielding material may be a shaped metal or an adhesive matrix with embedded tungsten particles, which attenuate the radiation. Space Electronics, Inc. developed the RAD-COAT conformal shielding material in conjunction with NASA LaRC. The effectiveness of RAD-COAT has been validated in extensive laboratory testing. In 1999, the RAD-COAT material will be validated in a space flight experiment on the STRV-1d mission. The instrument radiation environment will be monitored using the radiation-monitor-on-a-chip technology. The measured environment will provide crucial data on the performance of the radiation shielding integrated into the structure and multifunction composite modules for future geostationary system designs.

5.4 Thermal

The operating temperature of these IR FPAs is ≈ 120 K and can be practically cooled using advanced radiator technology. The size and mass of the cooler may be reduced using materials advances such as carbon-carbon matrixes or AlBeMET. Carbon-carbon (C-C) radiators are being developed for efficient thermal management of spacecraft subsystems and instrument electronics. C-C is a composite material that is lightweight, and has very high thermal conductivity (about 2 times that of copper). A C-C radiator weighs about 40 percent less than a conventional aluminum radiator of the same size. C-C radiator demonstration panels will be flown on the NMP EO-1 mission. AlBeMET has good properties for low temperature radiators. Its conductivity is near copper at cryogenic temperature with about 75% the density of aluminum and it has high stiffness and structural strength. In some applications this combination provides superior performance relative to more attractive materials with a more limited thermal range. A preliminary analysis indicates that these materials can yield a 50% reduction in radiative cooler mass.

5.5 Software

In order to achieve revolutionary improvements in software and system performance, the sensor software shall be designed with a high level of software system modularity, integration, and autonomy. Traditionally, each instrument has

required a unique software application associated with a unique set of dedicated processor resources. This traditional approach generated a design tightly coupled to the instrument implementation limiting the instrument software's maintainability and adaptability. The Geo Tropsat sensor software system architecture will be designed to isolate the application software by utilizing POSIX 1003.1b real-time extensions to the embedded Real-Time Operating System (RTOS) micro-kernel architecture interfaces. This design approach will ensure a tightly cohesive and loosely coupled interface to the RTOS micro-kernel resources.

The software system analysis and design will use the real-time Unified Modeling Language (UML) to capture the sensor system requirements and design concepts. System determinism and schedulability analyses will be performed using the Rate Monotonic Analysis (RMA) method.

As an essential element of the embedded flight software, the Wind River System's commercial off-the-shelf RTOS, VxWorks, was selected as the real-time operating system for the sensor system design. VxWorks was selected for its proven performance, portability and associated development tools. The VxWorks scaleable micro-kernel will be used to control the sensor software system and provide interface abstraction to POSIX 1003.1b real-time extensions.

6. Conclusions and Recommendations

The system study has shown that an instrument to measure trace gases (CO, O₃, NO₂, SO₂, CH₄, N₂O, and aerosols) from geostationary orbit is currently feasible but would greatly benefit from advanced technologies. Current technology supports an instrument design with 1024x1024 CCDs and FPAs however the science would be significantly enhanced through the use of larger (2048x2048) detector arrays and improved detector performance. The two factors that affect the instrument design the most are the detector well depth and the detector operating temperatures. The instrument design would also benefit from additional advances in miniaturized electronics, the use of multifunctional composite structures, improved data compression, and real time data analysis.

Continued effort should be placed upon the development of the improved large format detectors and the related instrument technologies required to improve the instrument design (reduced mass and power). This effort should be continued with the development of a modular spread system to evaluate emergent technologies. The modular spread system should include the optical system, sensor, filters, instrument controller, and software. The modular design of the spread system will allow for the comparative hardware analysis between various technologies and the selection of the most cost effective technology. The spread system will evaluate the incorporation of emergent hardware and the requirements for next generation of an imaging radiometer. The evaluation of the instrument and technology capabilities should be demonstrated through laboratory testing.

In assessing the expansion of trace gas measurements to geostationary orbit, the study determined that significant benefits accrue to the scientific community if partnerships with the commercial communications industry can be developed. In these partnerships, commercial satellite owners could provide on-orbit service leases for small science payloads. NASA's technology program could enable such partnerships through the definition of available service envelopes for small secondary payloads on commercial communications satellites and the definition of standard available physical interface envelopes. In addition, NASA should work with the commercial satellite industry to identify excess satellite capacity, which could be acquired for secondary payload use on behalf of Earth science researchers. A significant number of discovery or technology demonstration missions could be enabled with this secondary payload approach, leading to wiser selections for any subsequent scientific satellite mission from GEO. The rapid development cycle of commercial spacecraft provides added impetus for rapid instrument technology demonstrations.

7. Appendix A -- Focal Plane Array (FPA) Technologies

A comprehensive review of the current state-of-the-art infrared (IR) detector technologies was undertaken. The review focussed on a broad wavelength range from 0.8 μm to 28 μm (Near IR - LWIR (long wavelength IR)). This review provides a better understanding of current and near term detector technology for the development of advanced, compact, low mass, and low power instruments to measure atmospheric trace gases from GEO.

Before considering any IR focal plane arrays for space applications, we need to examine some of the most important parameters that are related to FPA performance. These parameters include: 1) spectral range, 2) quantum efficiency, 3) dark current, 4) full well, 5) charge transfer efficiency (CTE), 6) linearity, 7) uniformity, 8) D^* , 9) pixel operability, and 10) thermal response. These parameters can be used to develop a figure of merit such as noise equivalent power (NEP), noise equivalent temperature difference (NE Δ T), and minimum resolvable temperature difference (MR Δ T) which can be used to compare the performance of FPAs.

The IR detectors have been classified into two main groups. One is thermal detectors that include thermocouples, thermopiles, bolometers, and pyroelectric detectors and the second is quantum detectors, which includes photoconductors and photovoltaic diodes [A-1].

7.1.1 Thermal Detectors

Selected thermal detectors and their performance properties are reviewed as follows:

7.1.1.1 Pyroelectric Detector:

Pyroelectric detectors are made of ferroelectric materials and several commercial products are available. For example, Spiricon Inc. has designed and manufactured both linear and 2-D arrays using LiTaO_3 (lithium tantalate). The wavelength range of the linear arrays is 190 nm to 400 μm . The wavelength response of the 2-D arrays covers from 190 nm to 354 nm then skips the visible range and works well again from 1.06 μm to 400 μm (Spiricon, Inc.). The format of this IR array detector is 124 x 124 pyroelectric elements with pixel dimensions of 100 x 100 μm giving an overall array size of 12.4 x 12.4 mm^2 . The NEP of this detector array is 45 nW/Hz and the saturation power is approximately 2.2 W/ cm^2 . Thus, the dynamic range of these detectors is approximately 5,000. The operating temperature range is from room temperature to approximately 60 $^\circ\text{C}$ and the read noise of this detector is around 2,000 electrons. The specifications of this pyroelectric focal plane array detector (personal communications) are shown in Table 7-7.

7.1.1.2 Microbolometer:

Honeywell manufactured the first uncooled micro-bolometer in 1979. Today, low weight, low cost, high reliability silicon micro-machined bolometer arrays are available and cover a broad wavelength range from 8 to 14 μm . They are also available

from a number of sources including Rockwell, Lockheed Martin, Boeing, Raytheon, and NEC. The key advantages of uncooled bolometers over conventional HgCdTe, InSb, and QWIP focal plane arrays include less vibration, no acoustic noise, and low power. The disadvantages are very low F#, less sensitivity than cooled arrays, and limited frame rates [A-7]. Lockheed Martin is developing an uncooled microbolometer with a 327 x 245 array format [A-8] and with an infrared absorption of 80%. The pixel pitch is 46.25 μm , the frame rate is 60 Hz and the integration times is 14 ms. Raytheon Santa Barbara Research Center (SBRC) has successfully built a 320 x 240 array [A-9] with pixel size 48 μm x 48 μm , a frame rate of 60 Hz, and an operating temperature of 300 K. NEC has fabricated a Titanium bolometer array with 128 x 128 pixels [A-10]. The thermal conductance is 0.20 $\mu\text{W}/\text{K}$ with a fill factor of 59%, a frame rate of 30 Hz and an integration times 5.3 μs . The specifications and characteristics for these thermal detectors are compiled in Table 7-7. Table 7-1 shows the operational parameters of thermal detectors.

Table 7-1. Thermal Detector Performance and Operation Parameters

Detector Type	Operation Temp.(K)	Time Constant (ms)	Usable wavelength (μm)	D*(500K) ($\text{cm}\sqrt{\text{Hz}}/\text{W}$)
Thermocouples	300	10 - 100	0.8 - 20	$\leq 1.5 \times 10^9$
Thermopiles	300	0.5 - 400	0.8 - 35	$< 5 \times 10^9$
Bolometers	300	1 - 100	0.8 - 40	$< 5 \times 10^9$
Superconductor-B.	< 80	~ 0.5	1 - 1000	$\sim 1 \times 10^{10}$
Pyroelectric	300	0.1 - 100	0.6 - 35	$\leq 8 \times 10^8$

7.1.2 Quantum Detectors

A variety of quantum detectors and detector arrays are manufactured from different materials (e.g. PtSi, HgCdTe, GaAs/AlGaAs, InSb, InGaAs, PbS, PbSe, Si:Ga) by different companies. Their characteristic properties are discussed below.

7.1.2.1 PtSi: Platinum Silicide

Several manufacturers offer PtSi IR focal plane arrays. This material delivers detectors with high performance, low power, compact size, and low cost. Cameras made with PtSi Schottky Barrier FPAs have excellent NE Δ T and high uniformity, but low quantum efficiency. PtSi arrays provide a large format with high dynamic range and wide-field operation.

David Sarnoff Research Center [A-11] has designed a 640 x 480 PtSi FPA utilizing 1.25 μm design rules to achieve a 50% fill factor, less than 0.07°C NE Δ T, greater than 1.5 million electrons saturation level, and less than 110 mW power dissipation.

Nikon Corp. [A-12] offers an 811 x 508 pixel PtSi-SB IR CCD with a 38.2% fill factor, 0.06K NE Δ T, and 0.9997 CTE at 80K.

Mitsubishi Electric Corp. provides a 1040 x 1040 PtSi FPA with a readout noise level around 30 electrons, quantum efficiency of 8% at 1.25 μm wavelength and 2% at

2.15 μm wavelength. It operates as a charge sweep device and is further described in reference A-13.

Eastman Kodak (personal communication) manufactures a 328 x 252 array with a typical quantum efficiency of 4.3×10^{-3} electron/photon in the photodiode at 4 microns. The readout is interlaced.

SBRC [A-9] offers a 256 x 256 array format with a noise level less than 200 electrons, a 60 Hz frame rate, a fill factor of 88%, and spectral range from 1 μm to 5.7 μm . It is presented in Table 7-7.

7.1.2.2 **HgCdTe:** (Mercury Cadmium Telluride)

$\text{Hg}_{1-x}\text{Cd}_x\text{Te}$ is widely used for manufacturing IR FPA detectors with variable band-gaps and different cutoff wavelengths. The HgCdTe detector's detectivity, D^* , depends on the detector cutoff wavelength and this cutoff wavelength depends on the material alloy composition. This material can be used for a wide range of the IR spectrum (1 - 25 μm) and operates over a temperature range from liquid nitrogen to room temperature with low noise and high quantum efficiency. It is desirable to operate the system at higher temperatures to eliminate the need for cryocooling. This improves the sensor reliability and reduces the power budget.

Rockwell Science Center manufactures a large format (up to 2048 x 2048) HgCdTe IR FPA detector with a wavelength range from 0.8 μm to 17 μm [web site].

Sofradir in France has fabricated 320 x 240 FPAs [A-14] with a pixel pitch 30 μm , frame rate 50 Hz and fill factor adjustable up to 100%.

Rockwell has designed 256 x 256 HgCdTe FPA on CdZnTe substrate with very low power and low noise at high temperature operation (up to 180K). A larger 1024 x 1024 HgCdTe FPA on Al_2O_3 (sapphire) substrate operates at 80K. It has a pixel pitch of 18 μm , a frame rate from 1 - 80 Hz, and a quantum efficiency around 65% [web site, Rockwell, personal communication].

Fermionics has demonstrated a 128 x 128 FPA (personal communication) with three different cutoff wavelengths at three different temperatures. These cutoff wavelengths are 1.8 μm at ice temperature, 12 μm at 77K, and 14 μm at less than 45K.

Finally, SBRC [A-9] manufactures a 256 x 256 FPA of with a frame rate variable to 120 Hz and pixel operability of 99%. Some of its important parameters and their specifications are discussed in Table 7-7.

7.1.2.3 **HgMnTe:** (Mercury Manganese Telluride)

Recently, there has been a growing interest in the development of HgMnTe photovoltaic diodes. This diode material ($\text{Hg}_{1-x}\text{Mn}_x\text{Te}$) has a cutoff wavelength that depends on the material alloy composition. Becla [A-15] at MIT (Massachusetts Institute of Technology) has developed photovoltaic HgMnTe detectors and produced good quality p-n HgMnTe and HgCdMnTe junctions. Brimrose Corporation of America has developed APDs (Avalanche Photodiodes) of HgMnTe for the detection of far IR with increasing speed and performance compared to its standard line of photovoltaic HgMnTe detectors [A-16, A-17]. They have demonstrated an avalanche gain for 7- μm detectors of more than 40, and better than 10 for 10.6- μm detectors. They

have shown that the D^* for the APDs are improved by a factor of 2 and the long-wavelength (10.6- μm) devices should operate at speeds up to 1 GHz. Becla [A-18] has indicated that HgMnTe and HgCdMnTe are comparable to HgCdTe detectors with similar bandgaps and perform near the theoretical limit of their photoelectric properties. Some of the characteristic properties of HgMnTe photovoltaic IR detectors are presented in Table 7-7.

7.1.2.4 AlGaAs/GaAs - QWIP (Quantum Well Infrared Photodetector):

There is currently great attention focused on GaAs/ $\text{Al}_x\text{Ga}_{1-x}\text{As}$ quantum-well infrared photodetectors. These devices work over the spectral range from 3 - 5 μm and from 8 - 14 μm . This material has excellent performance properties including radiation hardness, high uniformity, low noise, high sensitivity, high stability, and low power consumption. The drawback of QWIP detectors is that they operate at lower temperatures with lower quantum efficiency than HgCdTe detectors.

Gunapala and co-workers [A-19] at the Jet Propulsion Laboratory (JPL) have demonstrated a 256 x 256 QWIP FPA in an Amber hand-held camera. With this system they have demonstrated a peak detectivity of $2.3 \times 10^{11} \text{ cm}^2/\text{Hz}/\text{W}$ and NE Δ T of 40mK at an operating temperature of 70K. The frame rate of the camera is 60 Hz and the full well charge capacity is 9 million electrons 70K. They have measured a quantum efficiency of 6.9% for the FPA alone and 3% in the camera. A 15 μm 128 x 128 FPA with pixel pitch 50 μm , quantum efficiency 3% and frame rate 50 - 200 Hz is reported in reference A-10. A Raytheon Amber QWIP FPA Camera with 640 x 480 format operating at 9 μm , with 25 μm pixel pitch, 10% uncorrected nonuniformity, 0.1% corrected uniformity, quantum efficiency of 2.3%, and a frame rate 30 Hz at 70K are presented in reference A-20. GaAs/AlGaAs QWIPS are compared to HgCdTe arrays in Table 7-2.

Table 7-2. Comparison of HgCdTe FPAs and GaAs/AlGaAs QWIP Parameters [A-21]

Parameters	QWIP Value, Unit	HgCdTe/CdZnTe Value, Unit
Spectral band	8 - 10 μm	8 - 10.1 μm
Quantum Efficiency (%)	4	56
D^* , $\lambda_p(8.8\mu\text{m})$	$5 \times 10^9 \text{ cm}^2/\text{Hz}/\text{W}$ at 78K $1 \times 10^{10} \text{ cm}^2/\text{Hz}/\text{W}$ at 70K	$1 \times 10^{11} \text{ cm}^2/\text{Hz}/\text{W}$ at 78K
D^* operability(%w/ $D^* > 0.5D^*_{\text{mean}}$)	99	99.1
ϕ_b	$2 \times 10^{16} \text{ photons}/\text{cm}^2\text{s}$	$1.5 \times 10^{16} \text{ photons}/\text{cm}^2\text{s}$
Responsivity	0.08 (A/W)	4.5 (A/W)
Gain	0.3 at 2.14 V	---
NE Δ T	0.037K at 78K (50Hz) 0.014K at 70K	0.0051K
Array size	128 x 128	64 x 64
Pixel size	60 x 60 μm^2	60 x 60 μm^2

Parameters	QWIP Value, Unit	HgCdTe/CdZnTe Value, Unit
RoA	2×10^3 ohm-cm ² at 78K	10 ohm-cm ² at 78K
Responsivity Uniformity	sigma/ μ = 2%@78K = 4%@70K	6%
Residual Nonuniformity	<0.01	0.012

7.1.2.5 *InSb*: (Indium Antimonide)

Indium Antimonide (InSb) is utilized to build large format FPA detectors with high quantum efficiency, low dark current, and a large well capacity. The only drawback of this material is a relatively high noise level and required low temperature operation.

Goodnough and co-workers [A-22] have reported the performance parameters of 128 x 128 pixel InSb focal plane array detectors from Santa Barbara FPA (Lockheed Martin). They have demonstrated devices with wavelength ranges from 0.4 μ m to 5.35 μ m (no anti-reflection coating, quantum efficiency 65%) and from 1.0 μ m to 5.35 μ m (anti-reflection coated, quantum efficiency 85%). The full-well of these devices for fast frame operation is 8.4 million electrons and for snapshot operation 17 million electrons. The noise level less is than 300 electrons rms, the power dissipation less than 105 mW for a nominal operating temperature of 80K. These results are presented in reference A-22.

Cincinnati Electronics Corporation [A-23] has demonstrated a 256 x 256 FPA detector with a full-well capacity 850,000 electrons, a quantum efficiency of 60 to 80%, read noise of 200 electrons, and dark current 100 electrons/sec.

A 256 x 256 FPA from SBRC [A-9] with spectral range from 0.5 to 5.4 μ m, frame rate of 120 Hz, full well capacity of 10 million electrons, and quantum efficiency ~90% has also been reported. SBRC [A-24] has also designed and developed a 1024 x 1024 InSb FPA detector. The performance and specifications of this detector are discussed for a pixel size of 27 μ m², frame rate of 20 Hz, full well capacity of 300,000 electrons at 1.0 V bias or 200,000 electrons at 0.6 V bias. The wavelength range is from 0.9 μ m to 5 μ m and can be extended to the visible with special anti-reflection coatings. Dark currents less than 0.1 electron/sec, noise level less than 50 electrons rms, and quantum efficiency 85% average from 0.9 to 5.0 μ m are reported for this detector.

7.1.2.6 *InGaAs*: Indium Gallium Arsenide

In_xGa_{1-x}As is a variable band gap material used to design, fabricate, and manufacture photodiodes and focal plane arrays. As with HgCdTe different cutoff wavelengths are obtained by changing the composition of the material.

EG&G Judson has manufactured multiplexed InGaAs photodiode arrays and extended wavelength InGaAs photodiodes. The wavelength range for multiplexed InGaAs device is from 0.8 μ m to 1.7 μ m with high resolution and wide dynamic range. The spectral range of the extended wavelength detector is from 0.8 μ m to 2.6 μ m with wide dynamic range, high linearity, and no cooling required. Typical specifications of multiplexed InGaAs photodiode arrays with operating temperature at 300K include

dark current of ± 2 pA and ± 5 pA, responsivity 0.8 A/W at 1300 nm, response non-uniformity less than 2%, and noise equivalent temperature of 1.8 fC. The specifications for the extended wavelength InGaAs photodiode with operating temperature at 300K are dark current from 40 to 100 μ A and responsivity 1.2 A/W at 2.25 μ m wavelength [EG &G Judson Catalog].

7.1.2.7 **PbS**: Lead Sulphide & **PbSe**: Lead Selenide

PbS and PbSe detectors used for many applications due to their excellent wavelength response range of 1 - 3 μ m and 3 - 5 μ m, respectively. The infrared detectors made from these materials are cost-effective, easy to produce, and flexible. The detector operating characteristics are a function of temperature [A-25]. For example, with PbS, as one changes the operating temperature from 77K to 298K, the spectral response changes from 1 - 4.5 μ m to 1 - 3 μ m, the peak wavelength shifts from 3.4 μ m to 2.5 μ m and the detectivity drops from 0.5 - 5 $\times 10^{11}$ to 0.1 - 1.5 $\times 10^{11}$ cm $\sqrt{\text{Hz}}/\text{W}$. For PbSe, the spectral range changes from 1 - 7 μ m to 1 - 4.8 μ m, the peak wavelength shifts from 5.2 μ m to 4.3 μ m, and the detectivity drops from 0.7 - 5 $\times 10^{10}$ to 0.05-0.8 $\times 10^{10}$ cm $\sqrt{\text{Hz}}/\text{W}$. PbS and PbSe detectors are often used as linear arrays. The high impedance of PbS and PbSe photoconductive devices allow them to be interfaced with CMOS readout circuits. Linear array formats with CMOS readouts are currently available in 64, 128, and 256-element configurations [A-26]. A summary of the performance of PbSe 38 x 56 arrays with pixel spacing of 51 μ m, dynamic range of 2000, and uniformity less than 20% is found in Table 7-7.

7.1.2.8 **Si:Ga** (Gallium Doped Silicon) and **Si:As** (Arsenic Doped Si)

The hybrid 58 x 62 Si:Ga array detectors and 320 x 240 Si:As IBC (impurity band conduction) Astronomy Focal Plane Array are manufactured by Raytheon SBRC. The hybrid 58 x 62 Si:Ga of SBRC with direct readout array [A-27], pixel center spacing 75 μ m, pixel active area 5.1 $\times 10^5$ cm 2 , well capacity 0.7 million electrons, and dark current less than 630 electrons/sec is stated. The 320 x 240 Si:As IBC Astronomy FPA [A-9] with full well 45 million electrons or 14 million electrons (switchable), frame rate 350 Hz, integration times 12 μ s, and operating temperature 4 - 10K are discussed in Table 7-7.

The Wide-field Infrared Explorer imaging system is developed by Rockwell Science Center, Anaheim CA [A-28] using the Si:Ga material. A 128 x 128 array format of WIRE Imaging System and its performance specifications are discussed with the spectral band1 (9 - 15 μ m) and band2 (21 - 27 μ m), pixel size 75 μ m, 100% fill factor, dark current less than 500 electrons/sec, and quantum efficiency 25% at 25 μ m and 20% at 12 μ m.

7.1.2.9 **Ge:Ga** (Gallium Doped Germanium)

The extrinsic semiconductor gallium doped germanium provides a very broad wavelength range from 50 to 200 microns. This semiconductor material is used for a number of space science and Earth science spaceflight missions.

Boeing Electronics System and Missiles Defense has manufactured a few detectors based on this material for JPL (personal contact). JPL used this product for the Multiband Imaging Photometer (MIPS) for SIRTf (Space Infrared Telescope Facility) and will provide long wavelength imaging between 12 and 180 μm [A-29]. Some specifications and their properties are discussed briefly in Table 7-7. The performance of some intrinsic quantum detectors is shown in Table 7-3 and the performance of some extrinsic quantum detectors is shown in Table 7-4. The parameters of IRCCDs are shown in Table 7-5.

Table 7-3. Performance and Operation Parameters of Some Intrinsic Quantum Detectors [A-1]

Detector Material	Operation Mode	Operation Temp. (K)	Time Constant (μs)	Peak Wavelength (μm)	Usable Wavelength (μm)	D*(500K) ($\text{cm}^2\sqrt{\text{Hz/W}}$)
Si	PV	300	10^{-2}	0.9	0.6 - 1.1	$\sim 10^7$
Si	Avalanche	300	$\sim 10^{-5}$	0.9	0.6 - 1.1	$> 2 \times 10^7$
Ge	PV	300	$\sim 10^{-5}$	1.5	0.9 - 1.9	5×10^9
PbS	PC	300	> 100	2.4	1.1 - 3.5	1.5×10^9
PtSi	Schottky Barrier	< 90	~ 1000	0.9	0.8 - 5.0	2×10^9
PbSe	PC	300	1-5	3.9	1 - 5.0	2×10^8
InSb	PV	77	0.1 - 2	4.9	2 - 5.5	5×10^{10}
CdHgTe	PV	195	~ 2	4.5	1 - 5.5	4×10^{10}
CdHgTe	PC	77	0.1 - 2	10.5	8 - 14	2.5×10^{10}
CdHgTe	PV	77	0.5 - 2	10.5	8 - 11.5	2×10^{10}
PbSnTe	PV	77	~ 0.5	11	8 - 11.5	2×10^{10}

Table 7-4. Performance and Operation Parameters of Some Extrinsic Quantum Detectors [A-1]

Material/Dopant	Operation Temp.(K)	Time Constant (ns)	Peak Wavelength (μm)	Usable Wavelength (μm)	D*(500K) ($\text{cm}^2\sqrt{\text{Hz/W}}$)
Si:Zn	70 - 110	10 - 50	2.4	0.9 - 2.5	8×10^9
Si:Te	< 120	50 - 100	3.5	0.9 - 4.2	2×10^{10}
Si:In	≤ 50	~ 100	4.6	0.9 - 7	2×10^{10}
Si:Mg	< 50	~ 5	11.5	0.9 - 12	5×10^{10}
Si:Ga	< 30	~ 50	15	0.9 - 17	2.5×10^{10}
Si:Bi	< 30	1 - 10	17.5	0.9 - 22	2.5×10^{10}
Si:As	< 30	~ 100	24	0.9 - 28	1.0×10^{10}
Ge:Cu	4.2	1 - 10	21	1.5 - 27	1.0×10^{10}
Ge:Zn	4.2	0.5 - 5	37	1.5 - 45	2.5×10^{10}
Ge:Be	4.2	0.1 - 10	50	1.5 - 65	BLIP

Material/ Dopant	Operation Temp.(K)	Time Constant (ns)	Peak Wavelength (μm)	Usable Wavelength (μm)	D*(500K) ($\text{cm}^2/\text{Hz}/\text{W}$)
Ge:Cd	4.2	1 - 50	90	1.5 - 100	BLIP
Ge:In (stressed)	4.2	1 - 10	110	1.5 - 240	BLIP (background- limited performance)

Table 7-5. IRCCD Detectors for Mid- and Long-Wavelength IR [A-1]

Detector Material	Spectral Band (μm)	Operation Temp.(K)	Element Number	Pixel Size (μm^2)	Fill Factor (%)
InSb	3 - 5	70 - 85	256x256	50x50	>85
			512x512	25x25	>80
			1024x1		100
CdHgTe	3 - 5	195	256x256	40x40	>60
			512x512 (under development)	27x27	>65
PtSi Schottky Barrier	3 - 7	40 - 90	512x512	32x25	66
			640x480	20x20	80
			1040x1040	17x17	71
Si:In	3 - 7	<50	128x128	50x50	>90
GaAs/AlGaAs Quantum-well	7 - 11	77	256x256	50x50	>65
CdHgTe	8 - 12	77	256x256	40x40	>75
			640x480	27x27	>70
Si:Ga	8 - 17	<30	128x128	75x75	>90
Si:Sb	12 - 36	<30	128x128	25x35	>90
Pyroelectric Lithium Tantalate	1 - 30	~300	192x128	35x35	>65

A comparison of IR imagers' costs with cryogenic or thermoelectric coolers [A-30] is presented in Table 7-6.

Table 7-6. Comparison of IR imagers cost

Feature	Present scanned cryogenic imagers	Cryogenic staring imagers	Uncooled Si microbolometer imagers
Aproximate system cost	\$100,000 (military volume production)	\$100,000 (military volume production)	\$1000 (high-volume production)
Typical focal plane	100 K	100 K	Room Temperature

Feature	Present scanned cryogenic imagers	Cryogenic staring imagers	Uncooled Si microbolometer imagers
temperature			
IR sensor	HgCdTe, InSb	HgCdTe, InSb, PtSi, GaAs/AlGaAs	Micromachined silicon
Typical NE Δ T	0.1 degree C	0.01 degree C	0.05 degree C
Applications	Military and specialized industrial applications	Military and specialized industrial applications	Widespread applications for military, commerce, research, industry, etc.

Table 7-7. Comparison of different IR FPAs imagers and their materials with specifications, costs, and their manufacturers.

Detector Material	Array Size	Pixel Size (μm^2)	Full Well Capacity (Me)	Detectivity, D^* ($\text{cm}^2/\text{Hz/W}$)	Operating Temperature	Spectral Range (μm)	Approximate Cost of FPA Detector	Manufacturers
Pyroelectric (LiTaO ₃)	124x124	100x100		2×10^5	Room temp. to -60°C	0.19 - 400	A-grade cost \$20K (10 - 15 bad pixels) B-grade cost \$15K (20 - 30 bad pixels)	Spiricon, Inc
Microbolometer	128x128 320x240 327x245 640x480	40x40 28x28			300K 300K 300K 300K	8 - 14 8 - 14 8 - 14 7.5 - 14	\$5K - \$10K \$10K - \$15K	NEC Corp. Raytheon (SBRC) Lockheed Martin Lockheed Martin
PtSi	256x256 328x252 640x480 811x508 1040x1040	30x30 27.5 24x24 18x21 17x17	0.9 1.5 0.75		79K 68 - 78K 40 - 80K 80K 60K	1 - 5.7 3.5 - 5 3 - 5 3 - 5 3 - 5	1024x1024 cost \$1-2M for 18-24 months	Raytheon (SBRC) Eastman Kodak Dav. Sarnoff Res. Ctre. Nikon Corp. Mitsubishi Elec. Corp.
HgCdTe	128x128 256x256 256x256 320x240 320x256 640x480 1024x1024	40x40 30x30 40x40 30x30 30x30 20x20 18x18	8 1 31 1 6 0.1 - 3	$\sim 5 \times 10^{11}$ $\sim 1 \times 10^{14}$	ice - 44K 77 - 100K $\sim 180\text{K}$ 90K - 130K 40 - 220K 78 - 80K $\sim 150\text{K}$	1.8 - 14 8.5 - 11 0.85 - 10 3-5&8-12 1.5 - 14 1 - 10 0.8 - 17	\$175K FPA Camera with electronics \$50K FPA for 3 - 6 months \$300K FPA Camera with electronics	Fermionics Raytheon (SBRC) Rockwell Int. Corp. Sofradir (France) Fermionics, Inc. Raytheon (SBRC) Rockwell Int. Corp.
HgMnTe	32 Linear Array 16 Linear Array			$(1 - 3) \times 10^{11}$ $(2 - 3) \times 10^{10}$	77K 77K	2 - 14 2 - 12	\$3.5K - \$4.2K for 1 month	Brimrose Corp. of America Collaborate with Massachusetts Institute of Technology

Detector Material	Array Size	Pixel Size (μm^2)	Full Well Capacity (Me)	Detectivity, D^* ($\text{cm}\sqrt{\text{Hz/W}}$)	Operating Temperature	Spectral Range (μm)	Approximate Cost of FPA Detector	Manufacturers
AlGaAs/GaAs	128x128 256x256 640x480 640x512	38x38 28x28 18x18 23x23	6 - 12 6 - 12	1.6×10^{10} 2.3×10^{11} 1.8×10^{11} 2.0×10^{11}	55K ~68K >70K >70K	8 - 17 8 - 14 5 - 20 5 - 23	\$200K under development	Raytheon-Amber-JPL Raytheon - Amber-JPL Raytheon - Amber-JPL JPL
InSb	256x256 256x256 640x512 640x512 1024x1024 1024x1024 1280x1024	30x30 24x24 28x28 27x27 20x20 20x20	0.85 10 8.4 8 0.3	$\sim 10^{12}$	4 - 77K 80K 80K 77K 35K ~77K ~77K	1 - 5.5 0.5 - 5.4 4 - 5.35 1 - 5.5 0.6 - 5 0.4 - 5.35 0.4 - 5.35	\$80K camera ready \$150K - \$160K camera \$250K for 14 months delivery ~\$160K camera ready late summer ~\$180K camera ready late summer	Cincinnati Elec. Corp. Raytheon (SBRC) Lockheed Martin (SBFP) Cincinnati Elec. Corp. Raytheon (SBRC) Lockheed Martin (SBFP) Lockheed Martin (SBFP)
InGaAs	128x128 320x240 320x256	60x60 40x40 30x30	5.0 >10 1	$\sim 1 \times 10^{13}$ $> 10^{12}$	25 °C 0 - 40 °C 220 - 250K	0.9 - 1.7 0.9 - 1.7 0.9 - 1.7	\$20K FPA. For cutoff wavelength 2.5 μm cost \$1M for 24 months. \$40K FPA for 3 - 6 months	Sensors Unlimited Sensors Unlimited Fermionics, Inc
PbS	64x64 256 linear array	0.005^{m^2} 100x250 0		$\geq 8 \times 10^{10}$ 2×10^{11}	300K 300K	1 - 3 1 - 3	\$8K with multiplexing electronics \$7K-8K with multiplexing electronics (2 months)	N. E. Photoconductor SensArray Corporation
PbSe	64, 128, 256 linear array 256 linear array	38x56 100x250 0		$> 3 \times 10^{10}$ $\sim 10^{10}$	77K 300K	3 - 6 2.5 - 5	\$7K-8K with multiplexing electronics (2 months)	Litton Electron Devices SensArray Corporation
Si:Ga	58x62 128x128	75x75	0.7		7.5K	5 - 17 9 - 27		Raytheon (SBRC) Raytheon (SBRC)
Si:As Si:As Si:As IBC Si:As	256x256 256x256 320x240 512x412	50x50 30x30 50x50 30x30	0.03 - 0.05 0.03 45 or 14		10 - 15K 6 - 8K 12K 6 - 8K	2 - 28 2 - 28 10 - 24 2 - 28	Unoptimized cost \$100K \$95K for 14 months delivery \$95K for 12 months delivery \$120K for 12 months delivery	Boeing ESMD (RTC) Raytheon (SBRC) Raytheon (SBRC) Raytheon (SBRC)

Detector Material	Array Size	Pixel Size (μm^2)	Full Well Capacity (Me⁻)	Detectivity, D* (cm²/Hz/W)	Operating Temperature	Spectral Range (μm)	Approximate Cost of FPA Detector	Manufacturers
Si:As	1024x1024 1024x1024	18x18 27x27	0.03 0.1 0.03		10 - 15K 6 - 8K	2 - 28 2 - 28	Unoptimized cost \$150K \$250K for 24 months delivery	Boeing ESMD (RTC) Raytheon (SBRC)
Ge:Ga	5 elements	100x100			2K	50 - 200		Boeing ESMD (RTC)

7.2 Discussion and Summary

The main goal of this study report was to document the current status of infrared focal plane array technology, FPA performance, and to select a FPA technology for Geo Tropsat. The selected FPA technology was determined by the Geo Tropsat requirements.

The study has shown that HgCdTe is one of the most mature materials with high performance large format IR FPAs with a moderate operating temperature, low noise, desirable spectral range, and is scaleable to larger formats. Preliminary research has shown that HgZnTe can replace HgCdTe in applications for further improvement of the mercury-based narrow gap materials. A literature survey showed that HgCdTe and HgZnTe photodiodes have comparable performance at 77K with a 10.5 μm cutoff wavelength, quantum efficiency 65% for HgZnTe and 62% for HgCdTe, and detectivity $(1.0 - 1.2) \times 10^{11} \text{ cm}\sqrt{\text{Hz}}/\text{W}$ for HgZnTe and $(1.1 - 1.4) \times 10^{11} \text{ cm}\sqrt{\text{Hz}}/\text{W}$ for HgCdTe of the sensitive area $50 \times 60 \mu\text{m}^2$ (31 - 32). The study also indicated that the currently immature GaAs/AlGaAs QWIP arrays may have advantages over other materials for low-background long-wavelength space applications in the future.

The FPA technologies and capabilities are summarized in Table 7-7. Finally, based-on the overall system study (i.e., low noise, high quantum efficiency, and desirable spectral range with moderate operating temperature) HgCdTe FPA technology is recommended

7.3 FPA References

- A-1. K.J. Stahl, "Infrared Detectors: Expanded Applications Prompt Developments in Technology," The Photonics Design and Applications Handbook, pp H-218 - H-220 (1997).
- A-2. T. Tanabe, S. Nishida, Y. Nakada, S. Matsumoto, T. Onaka, K. Sekiguchi, T. Ono, I.S. Glass, and D.B. Carter, "PANIC (PtSi Astronomical Near-Infrared Camera) in South Africa and Its Astronomical Applications," Proc. SPIE 2744, pp 110 - 114 (1996).
- A-3. E.E. Haller, M.R. Hueschen, and P.L. Richards, "Ge:Ga Photoconductors in low infrared backgrounds," Appl. Phys. Lett. 34(8), pp 495 - 497 (1979).
- A-4. J. Wolf, "Low-background far-infrared detectors and arrays," Opt. Eng., Vol 33(5), pp 1492 - 1500 (1994).
- A-5. C.H. Blazquez, H.N. Nigg, L.E. Hedley, L.E. Ramos, R.W. Sorrell, and S.E. Simpson, "First derivative vs absolute spectral reflectance of citrus varieties," Proc. SPIE 2744, pp 673 - 676 (1996).
- A-6. P.A. Jones, R.K. Jungquist, and C.S. King, "A spaceborne tactical sensor concept," Proc. SPIE 3061, pp 37 - 46 (1997).
- A-7. J.L. Miller, H. Duvoism III, and G. Wiltsey, "Helmet-mounted uncooled FPA camera for buried object detection," Proc. SPIE 3061, pp 224 - 235 (1997).
- A-8. C.A. Marshall, T. Breen, M. Kohin, W. Watson, R. Murphy, N.R. Butler, T.W. Parker, and L. Perich, "Quantitative and imaging performance of

- uncooled microbolometer sensors," Proc. SPIE 3061 (1), pp 191-197 (1997).
- A-9. Santa Barbara Research Center's (Part of Raytheon's) Web Site (1998).
- A-10. A. Tanaka, S. Matsumoto, N. Tsukamoto, S. Itoh, K. Chiba, T. Endoh, A. Nakazato, K. Okuyama, Y. Kumazawa, M. Hijikawa, H. Gotoh, T. Tanaka, and N. Teranishi, "Influence of Bias Heating on Titanium Bolometer Infrared Sensor," Proc. SPIE 3061, pp 198-209 (1997).
- A-11. T.S. Vilani, B.J. Esposito, T.J. Pletcher, D.J. Sauer, P.A. Levine, F.V. Shallcross, G.M. Meray, and J.R. Tower, "Performance of Generation III 640x480 PtSi MOS Array," Proc. SPIE 2225, pp 2-10 (1994).
- A-12. M. Shoda, K. Akagawa, and T. Kazama, "A 410K Pixel PtSi Schottky-Barrier Infrared CCD Image Sensor," Proc. SPIE 2744, pp 23-32 (1996).
- A-13. K. Yanagisawa, N. Itoh, and T. Ichikawa, "Evaluation of the 1040x1040 PtSi CSD for astronomical Use," Proc. SPIE 2744, pp 92-103 (1996).
- A-14. P. Tribolet, V. Compain, and R. Boch, "High performance MCT LWIR and MWIR staring array for high frame rate applications," Proc. SPIE 2744, pp 374-392 (1996).
- A-15. P. Becla, "Infrared photovoltaic detectors utilizing $Hg_{1-x}Mn_xTe$ and $Hg_{1-x-y}Cd_xMn_yTe$ alloys," J. Vac. Sci. Technol. A4, 2014 - 2018 (1986).
- A-16. H.W. Messenger, "Bigger seems to be better for modern detectors," Laser Focus World, pp 77 - 84 (1991).
- A-17. P. Becla, S. Motakef, and T. Koehler, "Long wavelength HgMnTe avalanche photodiodes," J. Vac. Sci. Technol. B 10(4), pp 1599 1601 (1992).
- A-18. P. Becla, "Advanced infrared photonic devices based on HgMnTe," Proc. SPIE 2021, pp 22 - 34 (1993).
- A-19. S.D. Gunapala, J.K. Liu, M. Sundaram, S.V. Bandara, C.A. Shott, T. Hoelter, P.D. Maker, "Long Wavelength Quantum Well Infrared Photodetector (QWIP) Research At Jet Propulsion Laboratory," Proc. SPIE 2744, pp. 722-730 (1996).
- A-20. S.D. Gunapala, S.D. Bandara, J.K. Liu, W. Hong, M. Sundaram, R. Carralejo, C.A. Shott, P.D. Maker, and R.E. Muller, "Long-wavelength 640x484 GaAs/Al_xGa_{1-x}As Quantum Well Infrared Photodetector Focal Plane array Camera," Proc. SPIE 3061, pp 722-727 (1997).
- A-21. R.E. DeWames, J.M. Arias, L.J. Kozlowski, and G.M. Williams, "An assessment of HgCdTe and GaAs/AlGaAs technologies for LWIR infrared images," Proc. SPIE 1735, 2-16(1992).
- A-22. M.A. Goodnough, L.J. Hahn, R.B. Jones, B.D. Rosner, and J.S. Stineman, "A Flexible 640x512 InSb FPA Architecture," Proc. SPIE 3061, pp 140 - 149 (1997).
- A-23. E. Joven, L.F. Rodriguez-Ramos, J.J. Diaz, A. Rodriguez-Mora, N.A. Sosa, M.R. Williams, F. Fuentes, E. Cadavid, A. Manescau, V. Sanchez, E. Paez, C. Martin, J.M. Rodriguez-Espinosa, P. Hammersley, and J.C. Gonzalez, "Electronic Testing of the IAC infrared camera," Proc. SPIE 2225, pp 193-204 (1994).
- A-24. A.M. Fowler, F.J. Vrba, and A. Hoffman, "ALADDIN, The 1024x1024 InSb Array: Design, Description, and Results," Proc. SPIE 2816, pp 150-160 (1996).

-
- A-25. R.E. Harris, "Lead-Salt Detectors," *Laser Focus/Electro-optics*, pp 87 - 96 (Dec. 1983).
- A-26. P.R. Norton, "Infrared Image Sensors," *Optical Eng.* 30, pp 1649 - 1663 (1991).
- A-27. D.Y. Gezari, W.C. Folz, L.A. Woods, and J.B. Wooldridge, "A 58x62 pixel Si:Ga array camera for 5-14 μm astronomical imaging", *Proc. SPIE* 973, 287-298 (1988).
- A-28. H. Schember, J.C. Kemp, H.O. Ames, P.B. Hacking, T.L. Herter, B. Fafaul, D. Everett, and L. Sparr, "The Wide-Field Infrared Explorer (WIRE)," *Proc. SPIE* 2744, pp. 751-760(1996)
- A-29. L. Simmons, J. Fanson, W. Irace, J. Kwok, and M. Werner, "SIRTF: The Fourth Great Observatory," *Proc. SPIE* 2744, pp 731 - 744 (1996).
- A-30. R.A. Wood and N.A. Foss, "Micromachined bolometer arrays achieve low cost imaging," *Laser Focus World*, pp 101-106 (June, 1993).
- A-31. R. Triboulet, M. Bourdillot, A. Durand, and T. Nguyen, "(HgZn)Te among the other materials for IR detection," *Proc. SPIE* 1106, pp. 40-47 (1989).
- A-32. A. Rogalski, "Infrared Photon Detectors," *SPIE - The International Society for Optical Engineering* (1995)

8. Appendix B: Charge Coupled Devices (CCDs) for the UV – Visible Spectrum

A review of the current state-of-the-art CCD technologies was undertaken. The review focussed on a wavelength range from 0.3 μm to 0.8 μm (UV - visible). This review provides a better understanding of current and near term detector technology for the development of an advanced, compact, low mass, and low power instrument to measure atmospheric trace gases from GEO. Present CCD detector status, specifications, cost, and vendors are shown in Table 8-1.

Table 8-1. Comparison of CCDs' Performance Parameters, Costs, Delivery Time, and Vendors

Manufacturers	Array Format	Pixel Size (μm^2)	Full Well Capacity (Me)	Spectral Range (μm)	Dark Current (pA/cm^2)	Read Noise (e^-)	Quantum Efficiency (%)	Charge Transfer Efficiency	Approximate cost of CCD
Eastman Kodak	1024x1024	24x24	0.25	0.4 - 1.05	10 - 30	20	30 - 40	0.9999	\$4K - 12K for 1 month \$40K depending on size and image quality for 6 to 18 months \$20K - 50K for 1 month
	1024x2048	10 to 24	0.25 - 0.50	0.4 - 1.05	10 - 30	20	30 - 40	~0.9999	
	2048x2048	10 to 24	0.25 - 0.50	0.4 - 1.05	10 - 30	20	30 - 40	~0.9999	
	2048x4096	10 to 24	0.25 - 0.50	0.4 - 1.05	10 - 30	20	30 - 40	~0.9999	
	4096x4096	9x9	0.085	0.4 - 1.05	10	<20	30 - 40	0.99999	
Dalsa Inc.	128x128	16x16		0.4 - 1.0				0.99995	\$2.95k for 1 month \$6.5K for 1 month \$5.9K - 7K for 1 month
	512x512								
	1024x1024	12x12	0.12 (max)	0.4 - 1.0		0.39mV(max. rms noise)		0.999995	
Lockheed Martin (Fairchild)	9216x9216	8.75x8.75		0.4 - 0.8	<100	<40	>35 (0.55 to 0.8 μm)	0.999995 (VCTE) 0.999995 (HCTE)	\$100K (in Stock)
Scientific Imaging Technologies, Inc. (SITE)	2048x2048	24x24	0.20	0.4 - 1.0	100-MPP 500-non	10	20 - 40 (@ 0.5 - 0.7 μm)	0.99999	Grade 1: 4 outputs cost \$75K Grade 1: 2 outputs cost \$65K
	2048x4096	15x15	0.20(serial)	0.4 - 1.0 (front side illumination)	100 (max - MPP)	7 e^- , rms (max)	20 - 40 (@ 0.5 - 0.7 μm)	0.99995 (min) @ 500 electrons	
EG&G, Inc., Reticon	1024x1024	9x9	<0.05		0.5 nA/cm^2	15 e^- , rms	20 @.45 μm 25 @.53 μm 25 @ 0.65		Grade 3: 2 outputs cost \$6.5K